Article

Vegetation Restoration Enhanced Canopy Interception and Soil Evaporation but Constrained Transpiration in Hekou–Longmen Section During 2000–2018

Peidong Han [1,2,†], Guang Yang [1,3,†], Yangyang Liu [1,2,4,*], Xu Chen [5,*], Zhongming Wen [1,2], Haijing Shi [1,3], Ercha Hu [4,6], Tingyi Xue [2] and Yinghan Zhao [2]

1 State Key Laboratory of Soil Erosion and Dryland Farming on the Loess Plateau, Institute of Water and Soil Conservation, Chinese Academy of Sciences and Ministry of Water Resources, Yangling 712100, China; 2022056886@nwafu.edu.cn (P.H.); elliott67@nwafu.edu.cn (G.Y.)
2 College of Grassland Agriculture, Northwest A&F University, Yangling 712100, China
3 State Key Laboratory of Soil Erosion and Dryland Farming on Loess Plateau, Institute of Soil and Water Conservation, Northwest A&F University, Yangling 712100, China
4 Inner Mongolia Daqingshan Forest Ecosystem National Observation and Research Station, Inner Mongolia Academy of Forestry Sciences, Hohhot 010010, China
5 College of Mechanical and Electronic Engineering, Northwest A&F University, Yangling 712100, China
6 Inner Mongolia Academy of Forestry Sciences, Hohhot 010010, China
* Correspondence: 2020110044@nwafu.edu.cn (Y.L.); chenxu@nwafu.edu.cn (X.C.)
† These authors contributed equally to this work.

Abstract: The quantitative assessment of the impact of vegetation restoration on evapotranspiration and its components is of great significance in developing sustainable ecological restoration strategies for water resources in a given region. In this study, we used the Priestley-Taylor Jet Pro-pulsion Laboratory (PT-JPL) to simulate the ET components in the Helong section (HLS) of the Yellow River basin. The effects of vegetation restoration on ET and its components, vegetation transpiration (Et), soil evaporation (Es), and canopy interception evaporation (Ei) were separated by manipulating model variables. Our findings are as follows: (1) The simulation results are compared with the ET calculated by water balance and the annual average ET of MODIS products. The R^2 of the validation results are 0.61 and 0.78, respectively. The results show that the PT-JPL model tracks the change in ET in the HLS well. During 2000–2018, the ET, Ei, and Es increased at a rate of 1.33, 0.87, and 2.99 mm/a, respectively, while the Et decreased at a rate of 2.52 mm/a. (2) Vegetation restoration increased the annual ET in the region from 331.26 mm (vegetation-unchanged scenario) to 338.85 mm (vegetation change scenario) during the study period, an increase of 2.3%. (3) TMP (temperature) and VPD (vapor pressure deficit) were the dominant factors affecting ET changes in most areas of the HLS. In more than 37.2% of the HLS, TMP dominated the change affecting ET, and vapor pressure difference (VPD) dominated the area affecting ET in 30.5% of the HLS. Overall, the precipitation (PRE) and VPD were the main factors affecting ET changes. Compared with previous studies that directly explore the relationship between many influencing factors and ET results through correlation research methods, our study uses control variables to obtain results under two different scenarios and then performs difference analysis. This method can reduce the excessive interference of influencing factors other than vegetation changes on the research results. Our findings can provide strategic support for future water resource management and sustainable vegetation restoration in the HLS region.

Keywords: evapotranspiration; PT-JPL model; climate change; vegetation restoration; structural equation model

1. Introduction

The hydrological cycle refers to the continuous and dynamic circulation of water within the Earth–atmosphere system, encompassing various processes such as evaporation,

condensation, and precipitation [1]. Within this cycle, evapotranspiration (ET) represents the second largest component of the terrestrial water cycle, following precipitation, and plays a crucial role in transferring water from the land surface to the atmosphere through both evaporation from soil and water bodies and transpiration from plants [2]. It is also the key link connecting the Earth's ecosystem, hydrological cycle, and biogeochemical cycle. In our special study, ET is divided into three main components: vegetation transpiration (Et), soil evaporation (Es), and canopy interception evaporation (Ei). Among these, Et is the most significant contributor to the total evapotranspiration in terrestrial ecosystems [3]. Research has demonstrated that the ET process is significantly influenced by regional climate variations and changes in terrestrial vegetation. Climate change directly impacts the ET process by altering the atmospheric water retention capacity, which in turn affects precipitation patterns, humidity levels, and the growth and distribution of vegetation, ultimately influencing the overall hydrological cycle [4]. At the same time, it may also lead to regional changes in soil moisture, thus indirectly affecting ET [5]. Vegetation is an important part of the terrestrial ecosystem and an important link between the energy circulation and material circulation between the soil circle, the hydrosphere, and the atmosphere [6]. Changes in surface vegetation play an important role in regulating water circulation, energy circulation, and global carbon balance on the land surface. On the other hand, vegetation will also have a dynamic response to the external environment through biophysical and biochemical pathways, in which vegetation can have a profound impact on the regional and even global carbon–water cycle system through photosynthesis and transpiration [7]. Vegetation can have a feedback effect on ET by intercepting precipitation, changing surface roughness, and affecting runoff patterns [8]. ET and vegetation are closely linked and interdependent through the balance mechanism of natural evolution. Large-scale vegetation restoration and greening projects have significantly changed surface characteristics while improving the health of the local ecosystem [9]. The influence of vegetation greening on ET exhibits considerable variations across different regions and time periods. For instance, in the Loess Plateau, vegetation greening and shifts contribute more to ET than climate change, whereas in certain areas of northern China, precipitation changes play a more pivotal role in impacting ET [10]. Therefore, accurately quantifying the specific effects of vegetation greening and change and climate change on ET is of irreplaceable significance for the scientific management and efficient use of regional water resources and the promotion of ecological sustainable development [11].

Accurately revealing the characteristic trend in vegetation change is the premise of understanding vegetation change. As science and technology advance, satellite remote sensing products are offering hydrological research data with unmatched spatial resolution. However, when studying the complex dynamics of the hydrological cycle and its spatial distribution characteristics, the ET data obtained by satellite sensors alone often seem to be insufficient [12], because although these data can provide a macro-perspective ET overview, it is difficult to reveal the intricate physical interaction mechanism between ET and key hydrological variables such as soil moisture, groundwater level, precipitation, and runoff, and it is more difficult to accurately predict the temporal evolution trend in ET on different spatial scales in the future [1]. This limitation has prompted the hydrological science community to continuously explore more detailed and comprehensive ET estimation methods. Therefore, the ETWatch model, generalized complementary relationship, TSEB, and some models created by team independent innovation came into being. They can use remote sensing products to achieve long-term and high-spatial-resolution evapotranspiration estimation: Cao et al. [13] utilized the ETWatch model to estimate the actual ET in the Loess Plateau in China from 2000 to 2020 and employed the generalized additive model to quantitatively assess the contributions of climate factors and human activities to changes in ETa. Using the ETWatch method and the Penman–Monteith equation, Ma et al. [14] estimated the daily ET over the Loess Plateau from 2000 to 2015. Li et al. [15] utilized the generalized complementary relationship to quantitatively assess the influence of climate change and vegetation restoration on the increase in ET across the Loess Plateau by establishing the

relationship between AC and climatic vegetation factors in 14 watersheds in the region from 1981 to 2014. Lv et al. [16] used the Zhang model to predict the actual ET on the Loess Plateau from 1986 to 2016, established a water balance equation, and quantitatively distinguished the response of ET to climate change and land use.

The National Aeronautics and Space Administration (NASA) tested three mainstream evapotranspiration algorithms (the PT-JPL algorithm, PM-MOD16 algorithm, and SEBS algorithm). The PT-JPL algorithm, which had the highest Nash efficiency coefficient and the lowest root mean square error (RMSE), was chosen as the global evapotranspiration retrieval algorithm for the ECOSTRESS experiment on the space station [17]. In addition, the PT-JPL model requires the least local measurement parameters and has been widely used in ET and its component simulation [11,17]. Our study area is located in arid and semi-arid regions. Due to the lack of detailed ground observation data, conventional ET and GPP estimation models are often limited. In this context, the PT-JPL model has shown significant advantages in a data-scarce environment. Using widely available remote sensing data and improving algorithms and integrating other estimation methods will greatly improve the accuracy of ET [11]. The model inherits the accuracy of the PT algorithm in estimating potential ET and further improves the accuracy and applicability of ET estimation by introducing advanced data processing technology and a model optimization strategy [18]. While maintaining high precision, the dependence on ground-measured data is relatively low, which greatly reduces the threshold and cost of model application, making it possible to promote its use in a wide range of areas [19]. In addition, the model also has strong prediction ability. Based on current and historical data, combined with the prediction of future climate change, the model can simulate the trend in ET in the next period of time and provide a scientific basis for water resource management, agricultural irrigation, ecological environment protection, and other strategies [20].

As an indispensable key river section in the middle and upper reaches of the Yellow River, the HLS is famous for its diverse geographical forms and complex hydrological ecosystems [21]. The HLS is a crucial component of the global and regional water cycle, serving as a significant source of water resources for the Yellow River. However, it has been affected by human activities such as natural erosion, overgrazing, and unreasonable water and soil resource development for a long time, resulting in intensified soil erosion and serious vegetation degradation. This poses a direct threat to regional ecological security and significantly affects the ecological quality of the lower Yellow River and the broader area [22]. In order to cope with this challenge, the Chinese government has adopted a series of ecological restoration and protection measures in the HLS since 2000, including the integration of soil and water conservation, returning farmland to forest and grassland, and ecological migration [23]. It has successfully enhanced regional vegetation coverage, notably reduced soil erosion, and contributed to the improvement of the ecosystem in the HLS. However, the road to ecological restoration is not smooth. In the process of pursuing vegetation greening, some areas fail to fully consider the adaptability of vegetation types and water resource conditions, resulting in the excessive consumption of water resources, especially the significant decline of shallow groundwater level, which in turn induces new ecological crises such as soil drying and the secondary degradation of vegetation, highlighting the extreme importance of maintaining vegetation greening and water resource balance in ecological restoration. Against the backdrop of global climate change, the ET process of the HLS has become more intricate. Consequently, the future ecological management of the HLS should prioritize scientific planning and adopt comprehensive strategies, aiming to achieve an optimal balance between vegetation restoration and water resource conservation [23].

Our study used the PT-JPL model to simulate the spatial and temporal changes in ET under the two scenarios of vegetation change and no vegetation change in the HLS from 2000 to 2018, in order to explore the impact of vegetation change on regional ET. This study has the following two objectives: (1) to explore the net effect of vegetation change on ET and its components in the HLS; (2) to use a variety of research methods to explore

the impact of climate change and vegetation restoration on ET in the HLS, determine the main influencing factors according to the region, provide insights for use in water resources management and vegetation protection and greening, and provide suggestions for the formulation of ecological greening strategies in different regions.

2. Materials and Methods

2.1. Overview of the Study Area

The HLS is the area between Hekou Town and Longmen in the middle reaches of the Yellow River in China. It is located between 35°40′−40°34′ N and 108°02′−112°44′ E, with an area of 112,900 square kilometers [24]. The terrain of the HLS is more complex, from the southern trough (381 m) to the northern high mountains (2746 m). This obvious elevation gradient has an important impact on the climate and vegetation distribution in the region [23]. The HLS has a temperate continental monsoon climate. The temperature is low in the northern mountainous area, with a minimum of −1.49 °C, while the temperature is high in the southern trough area, up to 14.47 °C. The precipitation in the northern region is relatively high, with a maximum of 609.82 mm, while the precipitation in the southern region is relatively low, with a minimum of 321.89 mm. The area is dominated by grassland, accounting for most of the area (91.82%), in addition to some woodland, shrubland, cultivated land, and water area (Figure 1).
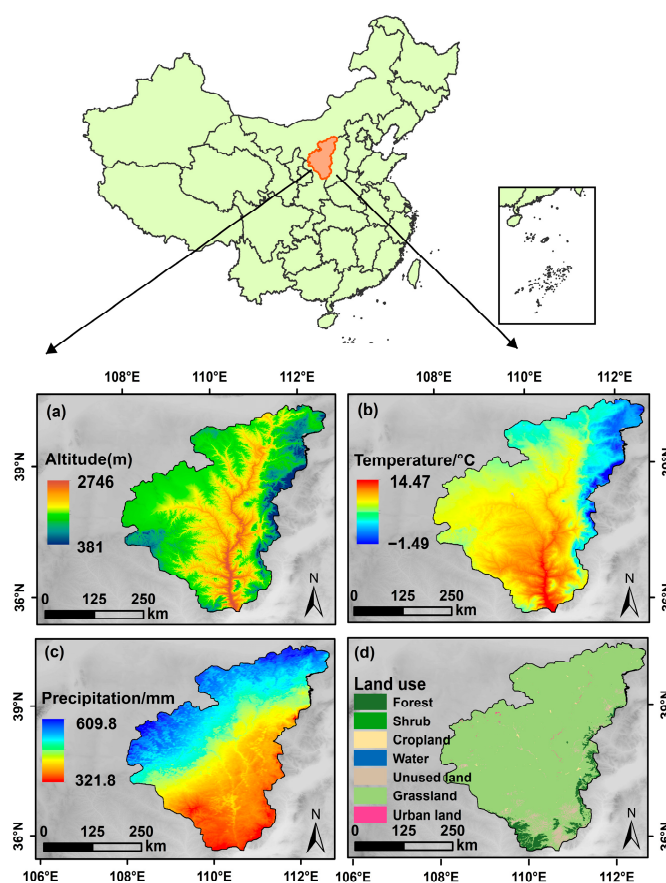

Figure 1. Overview of the Helong Section. (**a**) Elevation; (**b**) mean annual temperature; (**c**) mean annual precipitation; (**d**) land use/land cover types.

2.2. Data Sources and Our Processing

The datasets used in this study include satellite imagery datasets, vegetation datasets, land use/cover datasets, meteorological datasets, topography data, and other related underlying datasets (Table 1).

Table 1. All data sources used in the study.

Data	Spatial Resolution	Source
TMP (temperature)	500 m	Loess plateau science data center, National Earth System Science Data Sharing Infrastructure, National Science and Technology Infrastructure of China" http://loess.geodata.cn (accessed on 17 June 2024)".
NDVI (Normalized Difference Vegetation Index)	0.0833°	AVHRR GIMMS-3G+ "https://daac.ornl.gov/VEGETATION/guides/ Global_Veg_Greenness_GIMMS_3G.html (accessed on 11 June 2024)".
LAI (leaf area index)	0.05°	GLASS "https://glass-product.bnu.edu.cn/ (accessed on 2 March 2024)".
FVC (fractional vegetation cover)	0.05°	GLASS "https://glass-product.bnu.edu.cn/ (accessed on 2 March 2024)".
ET (evapotranspiration) for validation	500 m	MOD16A2—MODIS/Terra Net Evapotranspiration "https://ladsweb.modaps.eosdis.nasa.gov/missions- and-measurements/products/MOD16A2 (accessed on 10 June 2024)".
Land use/cover	1 km	National Earth System Science Data Center "https://www.geodata.cn/main/ (accessed on 2 June 2024)".
Meteorological data (PRE (precipitation) rate, TEM (surface temperature, °C), water vapor pressure (hPa), and near-surface pressure (Pa))	0.1°	China meteorological forcing dataset "https://data.tpdc.ac.cn/zh-hans/data/8028b944 -daaa-4511-8769-965612652c49/; (accessed on 2 March 2024)".
Albedo	0.05°	GLASS "https://glass-product.bnu.edu.cn/" (accessed on 2 March 2024)".
VPD (vapor pressure deficit)	0.5°	CLIMATIC RESEARCH UNIT "https://crudata.uea.ac.uk/ (accessed on 2 March 2024)"
Watershed boundary		National Earth System Science Data Center "https://www.geodata.cn/main/ (accessed on 17 June 2024)".
DEM (digital elevation model)	90 m	Geospatial Data Cloud "https://www.gscloud.cn/ (accessed on 2 March 2024)".

The RAD (radiation absorbed dose) that we used is also used in the later PT-JPL model [25]. The calculation equation is as follows:

$$R_{ns} = (R_n exp(-k_{R_n} LAI)) \tag{1}$$

$$R_{nc} = R_n - R_{ns} \tag{2}$$

$$R_n = R_{nshort} - R_{nlong} \tag{3}$$

$$R_{nshort} = (1-p)I_t \tag{4}$$

$$R_{nlong} = R_{ld} - R_{lu} \tag{5}$$

$$R_{lu} = \sigma T^4 \tag{6}$$

In these equations, R_{ns} represents the net radiation reaching the soil surface and R_{nc} represents the net radiation intercepted by the canopy; k_{R_n} represents the extinction coefficient with a value of 0.6 [11,26]; R_n is the net radiation, with R_{nshort} and R_{nlong} being the net shortwave radiation and net longwave radiation, respectively; p represents the surface albedo; I_t is the downward shortwave radiation; R_{ld} is the downward longwave radiation and R_{lu} is the upward longwave radiation; and σ is the Stefan–Boltzmann constant with the value of 5.67×10^{-8} W·m^{-2}. T represents the temperature (K) [27]. The units for all the radiation data used above are W·m^2.

The accuracy of CMFD data is 0.1°; although the accuracy is low, the dataset contains most of the data required in the PT-JPL model that we use, it has a unified data format and attributes, and it is specifically used for the simulation of land surface processes in China. The driving data will be very helpful for us in simulating the evapotranspiration of land surface processes in China. Another important data LAI could be obtained from the GLASS website of the University of Maryland before the start of research and analysis, but its LAI data as of 2018 have a resolution of 500 m. However, in the subsequent data analysis process, the processing methods that we use, especially multiple linear regression analysis, need to unify the resolution and range size of all data. At this time, the resolution of the VPD and water vapor pressure data available to us is low. However, in order to enable each datapoint to be processed and analyzed on a relatively more appropriate scale, we finally chose to compromise and unify the resolution of all data to 0.05° for all processes. Finally, all of the above raster data were resampled to 0.05° spatial resolution for subsequent use through the bilinear interpolation method of ArcMap 10.8 software [28].

2.3. Research Methods

2.3.1. ET Calculation Based on PT-JPL Model

In order to better simulate vegetation ET values, the PT-JPL [18] was developed as a GIS-based model by integrating remote sensing technology into vegetation dynamics to simulate ET values from the stand scale to the regional scale. The PT-JPL model divides ET into three components: *Et*, *Es*, and *Ei*. The following are the equations and parameters involved in the operation of this model:

$$ET = Et + Es + Ei \tag{7}$$

$$Et = (1 - f_{wet})f_g f_t f_m \alpha \frac{\Delta}{\Delta + \gamma} R_{nc} \tag{8}$$

$$Es = (1 - f_{wet} + f_{sm})(1 - f_{wet})\alpha \frac{\Delta}{\Delta + \gamma}(R_{ns} - G) \tag{9}$$

$$Ei = f_{wet}\alpha \frac{\Delta}{\Delta + \gamma} R_{nc} \tag{10}$$

In these equations, α is the PT coefficient with a value of 1.26 in our research; Δ is the slope of the VPD (kPa·°C^{-1}); γ is the psychrometric constant with the value of 0.066 (kPa·°C^{-1}) [27,29]; R_{nc} is the net radiation to the canopy (W·m^{-2}); R_{ns} is the net radiation to the soil (W·m^{-2}), *kRn* is the extinction coefficient with a value of 0.6 in our research. In the above equation, the other elements of the parameters and data used in the calculation equation are as follows:

$$f_{wet} = RH^4 \tag{11}$$

$$f_c = f_{IPAR} \tag{12}$$

$$f_g = \frac{f_{APAR}}{f_{IPAR}} \tag{13}$$

$$f_t = exp\left(-\left(\frac{T - T_{opt}}{T_{opt}^2}\right)^2\right) \tag{14}$$

$$f_m = \frac{f_{APAR} + 1}{f_{APARmax+1}} \tag{15}$$

$$f_{sm} = RH^{VPD/\beta} \tag{16}$$

$$f_{APAR} = b_1 \times (1 - \exp(-k_1 \times LAI)) \tag{17}$$

$$f_{IPAR} = b_2 \times (1 - \exp(-k_2 \times LAI)) \tag{18}$$

$$RH = 0.263 * shum * press * \left(exp\frac{17.67\,(T - T_0)}{T - 29.65} \right)^{-1} \tag{19}$$

$$G = R_n[\Gamma_c + (1 - M)(\Gamma_s - \Gamma_c)] \tag{20}$$

In these equations, f_{IPAR} is the proportion of PAR entrapped by the vegetation canopy. f_{APAR} is the proportion of $_{PAR}$ (photosynthetically active radiation) engrossed by the vegetation canopy [30]. During the calculation of f_{APAR} and f_{IPAR}, $b_1 = 0.95$ and $b_2 = 0.9355$ [19]. T_{opt} is the optimum temperature for plant growth; β is an index to indicate the sensitivity of soil moisture constraints to VPD in the range of 0–1; shum is the specific humidity, kg/kg; *press* is the near-surface pressure, Pa; T is the temperature, K; and T_0 is 273.16 K. G is the soil heat flux; Rn is the net radiation in the unit W·m^{-2}; and Γc and Γs are the parameters of the better vegetation coverage area and the better bare soil area with values of 0.05 and 0.325, respectively. M is the monthly vegetation coverage.

Different optimization and adjustment are needed in different studies. In our research, the parameters we use refer to Liu et al. [11] and Shao et al. [29], and then, after our adjustment, they are finally put into use. The specific parameter values used are shown in Table 2.

Table 2. Parameter values.

	k_1	k_2	beta (β)
forest	0.57	0.81	1.28
shrub	0.56	0.91	1.17
cropland	0.59	0.84	1.43
grassland	0.59	0.8	0.8

2.3.2. Indicators Used in the Verification of PT-JPL Model Results

For data validation, we selected the statistics of deviation Bias, RMSE (root mean square error) and intercepted to validate the results of our simulations [19,31]. The deviation Bias responds to the degree of deviation from the average of the two sets of data. It is calculated by the following equation [32]:

$$Bias = \frac{1}{n}\sum_{i=1}^{n} \left(\theta_i^{sim} - \theta_i^{obs} \right) \tag{21}$$

$$RMSE = \sqrt{\frac{1}{n}\sum_{i=1}^{n} \left[\theta_i^{obs} - \theta_i^{sim} \right]^2} \tag{22}$$

In these equations, n is the number of samples, θ_i^{sim} is the simulated value of the model, θ_i^{obs} is the measured value, *Bias* < 0 is the cold bias, and *Bias* > 0 is the warm bias [33].

We use the Pearson correlation coefficient R to indicate the degree of correlation between the PT-JPL simulation results and the MODIS ET, as well as the multi-year scale water balance ET, with values between -1 and 1. When $R = 1$, it means that the trends in the two types of data are exactly the same [34]. The calculation equation is as follows:

$$R = \frac{\sum(O_i - \overline{O})(M_i - \overline{M})}{\sqrt{\sum(O_i - \overline{O})^2 \sum(M_i - \overline{M})^2}} \tag{23}$$

In this equation, O_i represents the measured ET data, $\overline{O}$ is the mean value of the measured ET data, M_i is the ET of the regionally averaged PT-JPL simulation results, and $\overline{M}$ is the simulation results' mean value. Larger values for R indicate that the method is able to simulate its trends [35]. For the integration of long-term sequence data, we also use the 2D Smoother APP of Origin2024b software, specifically using the linear fitting function in

the Trendline part of this APP, which directly helped us to obtain the linear fitting equation and R^2 of long-term sequence data.

2.3.3. Scenario Designs

To investigate the effects of vegetation change on ET, we applied the PT-JPL model to simulate two different scenarios: one with varying vegetation cover (forest, grassland, farmland, shrubland) and one with constant vegetation cover. In the vegetation-change scenario, ET was calculated for normal vegetation development over time, while in the vegetation-invariant scenario, we assumed that the vegetation cover remained constant throughout the study period. Specifically, starting from 2000, we fixed the vegetation cover in the study area, disregarding changes in the environment, climate, or government ecological restoration policies, and kept the vegetation coverage at its 2000 levels. By comparing the results of the two scenarios, we were able to quantify the net impact of vegetation changes on ET in the TP between 2000 and 2018.

2.3.4. Trend Analysis Method

We analyzed the spatial and temporal trends in ET, Et, Ei, Es, and the two types of drivers (climate and vegetation) at the pixel level over the period 2000–2018 using the Mann–Kendall and Sen slope statistical tests [36].

$$\rho = median\frac{x_j - x_i}{j - i} \quad 1 < i < j < n \tag{24}$$

In the equation, n is the number of research years; xi is the NPP value of the i th year; and ρ is the trend degree, and when $\rho < 0$, it shows an upward trend [37].

$$Q = \sum_{i=1}^{n-1} \sum_{j=i+1}^{n} sign(x_j - x_i) \tag{25}$$

$$sign(xj - xi) = \begin{cases} 1 \ (xj - xi > 0) \\ 0 \ (xj - xi = 0) \\ -1 \ (xj - xi < 0) \end{cases} \tag{26}$$

$$Z = \begin{cases} \frac{Q-1}{\sqrt{Var(Q)}} \ (Q > 0) \\ 0 \ (Q = 0) \\ \frac{Q+1}{\sqrt{Var(Q)}} \ (Q < 0) \end{cases} \tag{27}$$

In these equations, Q is the statistic of the test; Z is the test statistic after standardization; and *var (Q)* is the variance. At a given significance level, if $Z < a/2$, it means that the significance test for the corresponding confidence has been passed. According to the results, the division standard is carried out as shown in Table 3.

Table 3. Trend test classification criteria that we used in all factors based on Sen and Mann–Kendall tests.

ρslope	Z Value	Trend
>0.0005	>1.96, <−1.96	Significantly increased
<0.0005	−1.96 < Z< 1.96	Significantly decreased
−0.0005 < ρ <0.0005	∞	Stably invariant
>0.0005	−1.96 < Z < 1.96	Minor increase
<0.0005	>1.96, <−1.96	Minor decrease

2.3.5. Attribution Analysis

We normalized the ET, Et, Ei, Es, PRE, TMP, RAD, and VPD using Equation (28) as a base and quantified the effects of all climates on ET, Et, Ei, and Es in the HLS using multiple

linear regression (MLR) [38]. Then, multiple regression analysis was performed on ET and its three components. The following equation was used:

$$X_i = \frac{x_i - x_{min}}{x_{max} - x_{min}} \tag{28}$$

$$Y_{ET} = b_0 + b_1 X_1 + b_2 X_2 + \cdots + b_i X_i + \mu \tag{29}$$

$$W_{ba_i} = \frac{b_i X_{i\_trend}}{Y_{ET_{a\_trend}}} Y_{ET_{n\_trend}} \tag{30}$$

In these equations, X_i is the value of the variable (normalized); x_i is the original value of the sequential data; x_{min} is the minimum value of the data; x_{max} is the maximum value of the sequential data; YET is the detrended ET, Et, Ei, and Es in the HLS (normalized); b_0 is the constant error; μ is the systemic error; and b_1–b_i are the standard regression coefficients. X_i represents the detrended climate variables and LAI (normalized), respectively; W_{bai} is the influence of each driving factor on ET change; and X_{i_trend}, Y_{ETa_trend}, and Y_{ETn_trend} are the trends in the driving variables, actual ET, and normalized ET, respectively.

We then apply the approach outlined by Sun et al. [39] to determine the dominant factors. For regions where the annual ET value rises, the factors contributing most positively to ET, namely, Et, Ei, Es within LAI, PRE, TEM, RAD, and VPD, are identified as the dominant factors [40].

2.3.6. Structural Equation Model (SEM)

The structural equation model (SEM) is a robust statistical method that allows for the quantification of dynamic interactions among multiple interconnected variables. This approach is especially advantageous in situations where traditional multiple linear regression analysis is insufficient, as it fails to accurately capture both the direct and indirect effects of vegetation and different environmental factors on ET and its components. By integrating latent variables and complex pathways, SEM offers a more thorough assessment of these interactions, providing deeper insights into fundamental ecological processes [41]. We used SEM to separate the direct and indirect effects of environmental variables on ET and its components based on SmartPLS 3. The accuracy and reliability of the model were evaluated by *GoF*. When *GoF* > 0.5, it shows that the model results are feasible. The calculation formula of *GoF* is as follows:

$$GoF = \sqrt{communality \times \overline{R^2}} \tag{31}$$

In the above equation, *communality* comes from the Q^2 value of the commonality of facet cross-validation, also known as common factor variance.

3. Results

3.1. Validation of the PT-JPL Model

3.1.1. Validation of Water Balance Method

The main runoff characteristic data in the HLS come from the two hydrological stations of Toudaoguai and Longmen. The two stations are the upstream gate station and the downstream gate station, which can represent the inflow and outflow of runoff in the study area. The calculation for interval runoff is the runoff of the downstream Longmen station minus the runoff of the upstream Toudaoguai station. The runoff for Toudaoguai and Longmen stations in 2000–2018 is shown in Figure 2a. The research shows that the average annual runoff of Toudaoguai hydrological station over 19 years is 16.845 billion m³, and the average annual runoff of Longmen hydrological station over the past 40 years is 18.901 billion m³. The average annual runoff of the study area over 19 years is 2.056 billion m3. The runoff depth of the HLS from 2000 to 2018 is calculated as shown in Figure 2b. The ET of the HLS from 2000 to 2018 was obtained by subtracting the average precipitation of

the HLS from 2000 to 2018 (Figure 2c). Figure 3 shows the validation comparison between the ET simulated by the model and the ET calculated by the water balance method.
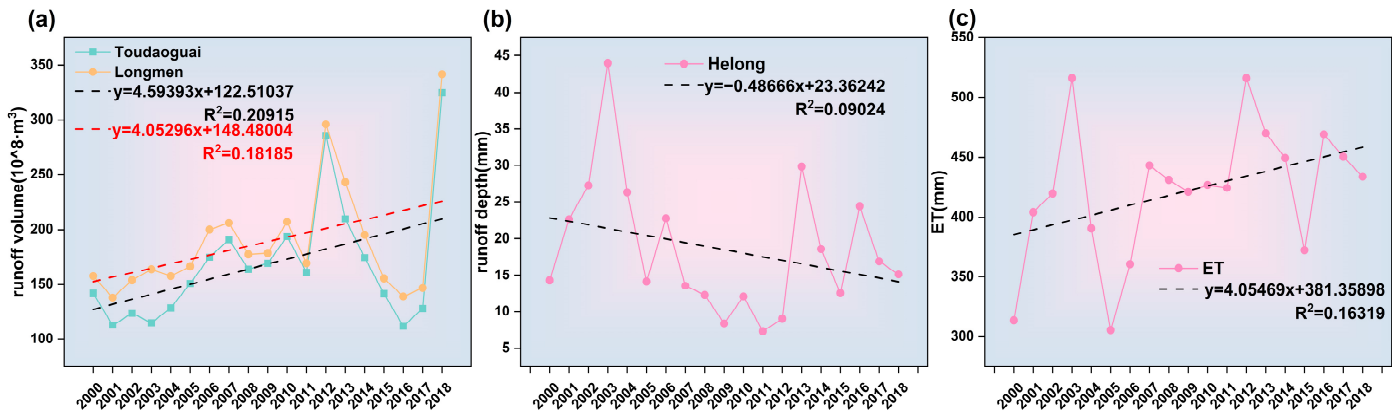

Figure 2. ET calculated by the water balance method in the HLS from 2000 to 2018. (**a**) The annual average runoff and its trend at the upstream and downstream gate stations. (**b**) The regional runoff of the HLS, obtained by subtracting the runoff of the upstream Toudaoguai station from the runoff of the downstream Longmen station. (**c**) The regional ET of the HLS, obtained by subtracting the regional runoff from the regional precipitation according to the water balance method.
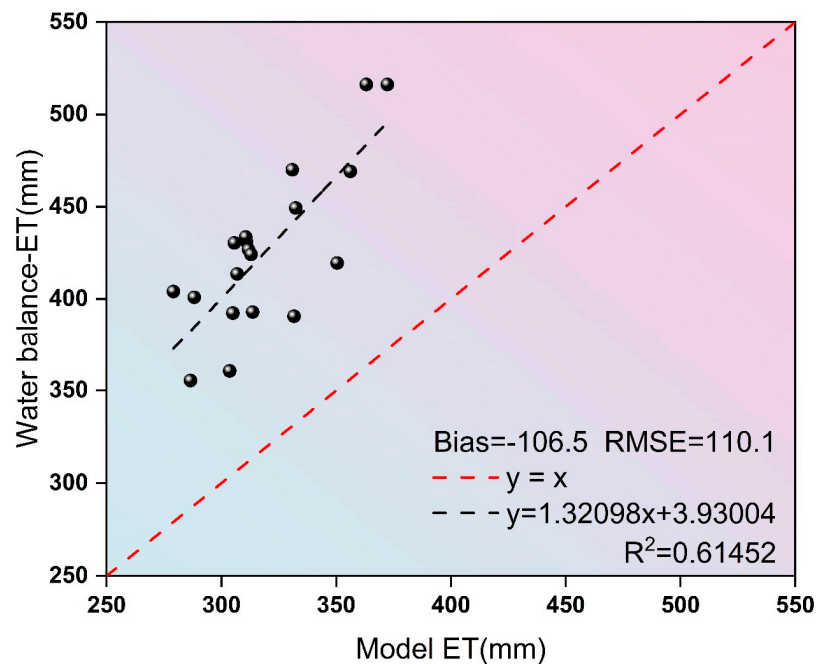

Figure 3. The results for ET simulated by PT-JPL and the water balance method (including Bias, RMSE, and linear fitting R^2 as indicators) are verified.

3.1.2. Validation of PT-JPL Model Based on MODSI ET

Figure 4 shows the annual ET data based on the PT-JPL model and MODIS products in the HLS, and the correlation analysis results between the two. Figure 4a shows the annual ET data based on the PT-JPL model. The simulated ET values of the model show obvious spatial differences over the range of the HLS. The ET value gradually decreases from the higher value (668.5 mm/a) in the north and middle to a lower value in the south. Figure 4b shows the annual ET data based on MODIS products. The ET values shown by MODIS products also have spatial heterogeneity, and the ET values gradually decrease from the higher values in the north and middle (815.7 mm/a) to the lower values in the

south (202.9 mm/a). Figure 4c shows the distribution of correlation coefficients between the PT-JPL model and MODIS products. The regions with strong correlations are predominantly located in the central and southwestern areas, where the correlation coefficients are generally high, around 0.94. This suggests a high level of consistency between the ET data from the PT-JPL model and MODIS products in these regions. Conversely, the areas with weaker correlations are mainly found in the southern and certain northern regions, with lower correlation coefficients, some even below 0.5, indicating notable differences in ET data between the PT-JPL model and MODIS products in these areas.
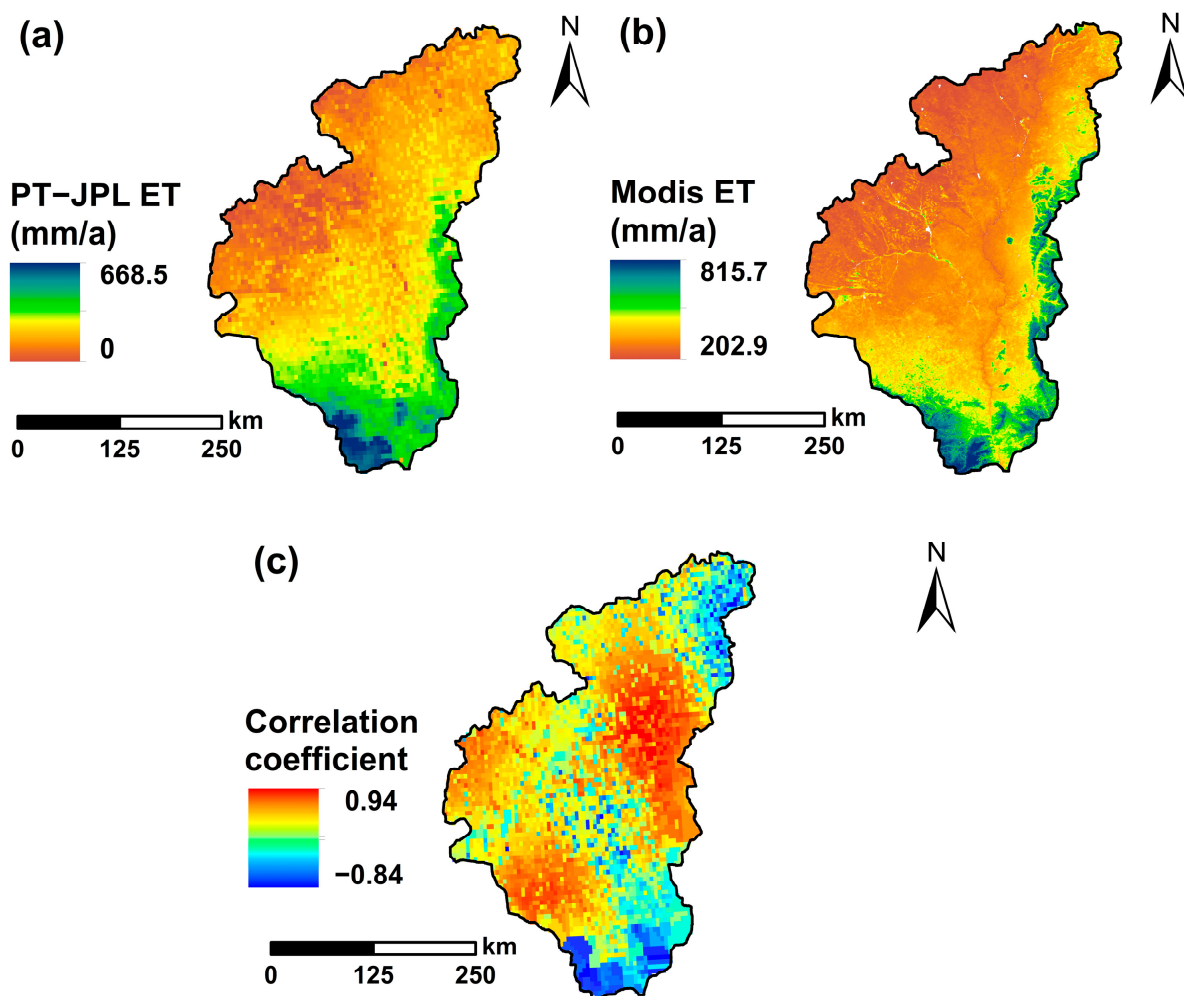

Figure 4. ET simulated by the PT-JPL model was verified by Modis ET. (**a**) Average ET simulated by the PT-JPL model from 2000 to 2018; (**b**) average Modis ET, 2000–2018; (**c**) the correlation between the multi-year average ET simulated by the PT-JPL model and the multi-year average ET of Modis was analyzed.

Furthermore, our research compared the annual ET simulated by the PT-JPL model with the annual ET from the MODIS product. The validation results indicated an R^2 value of 0.78, a Bias of 20.94 (Figure 5), and an RMSE of 44.79. The comparison between the annual average ET values from the PT-JPL model and those from the MODIS product demonstrates that the model's simulation results are highly reliable.
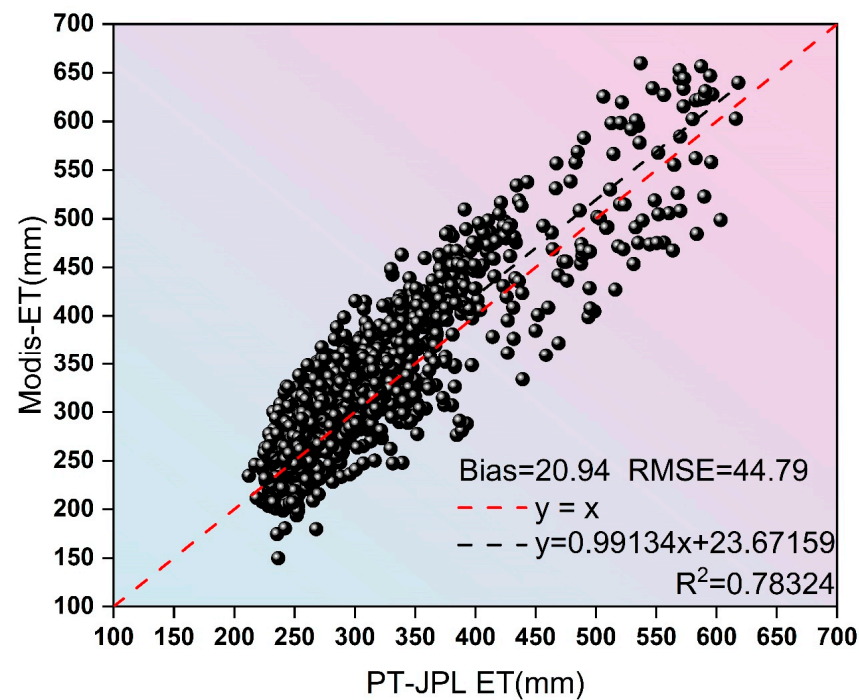
Figure 5. The annual verification results for ET and MODIS ET simulated by the PT-JPL model are verified year by year (including Bias, RMSE, and linear fitting R^2 as indicators).

3.2. Spatiotemporal Characteristics of Vegetation Change

Figure 6 illustrates the trend in NDVI and LAI in the HLS from 2000 to 2018, both of which surpassed the 95% significance threshold. Throughout the study period, most areas in the HLS experienced an upward trend in NDVI and LAI, with very few areas showing a decline. Figure 6c,d indicate that 92.03% of the NDVI in the HLS exhibited a significant increase, while 78.92% of the LAI showed a significant rise, closely linked to the implementation of the project aimed at converting farmland back to forests and grasslands. Grassland is the predominant land use type in the HLS, accounting for 91.82% of the area. The project focusing on the conversion of farmland to forest and grassland places a strong emphasis on the preservation and development of forested areas and grasslands, which has greatly contributed to the marked increase in NDVI and LAI. Specifically, this project not only enhances soil stability through the restoration of vegetation cover but also improves local microclimate conditions and bolsters the carbon sink function of the ecosystem. At the same time, this project also effectively reduces soil erosion and promotes the circulation and utilization of water resources. In addition, the restoration of grasslands and woodlands provides a good habitat for wildlife and further enhances regional biodiversity. The combined effects indicate that the initiative to convert farmland into forests and grasslands has been pivotal in enhancing the ecological environment of the HLS, leading to a substantial increase in NDVI and LAI. From the broken lines in the diagrams in Figure 6e,f, it can be seen that from 2000 to 2018, the annual NDVI and LAI in the HLS were in a fluctuating upward state, in which NDVI increased from 0.38 to 0.62. The linear fitting results showed that $R^2 = 0.79$, and the average increase rate was 0.009/a; the annual LAI value increased from 1.02 to 1.58, and the linear fitting result was good ($R^2 = 0.87$), with an average increase rate of 0.035/a.
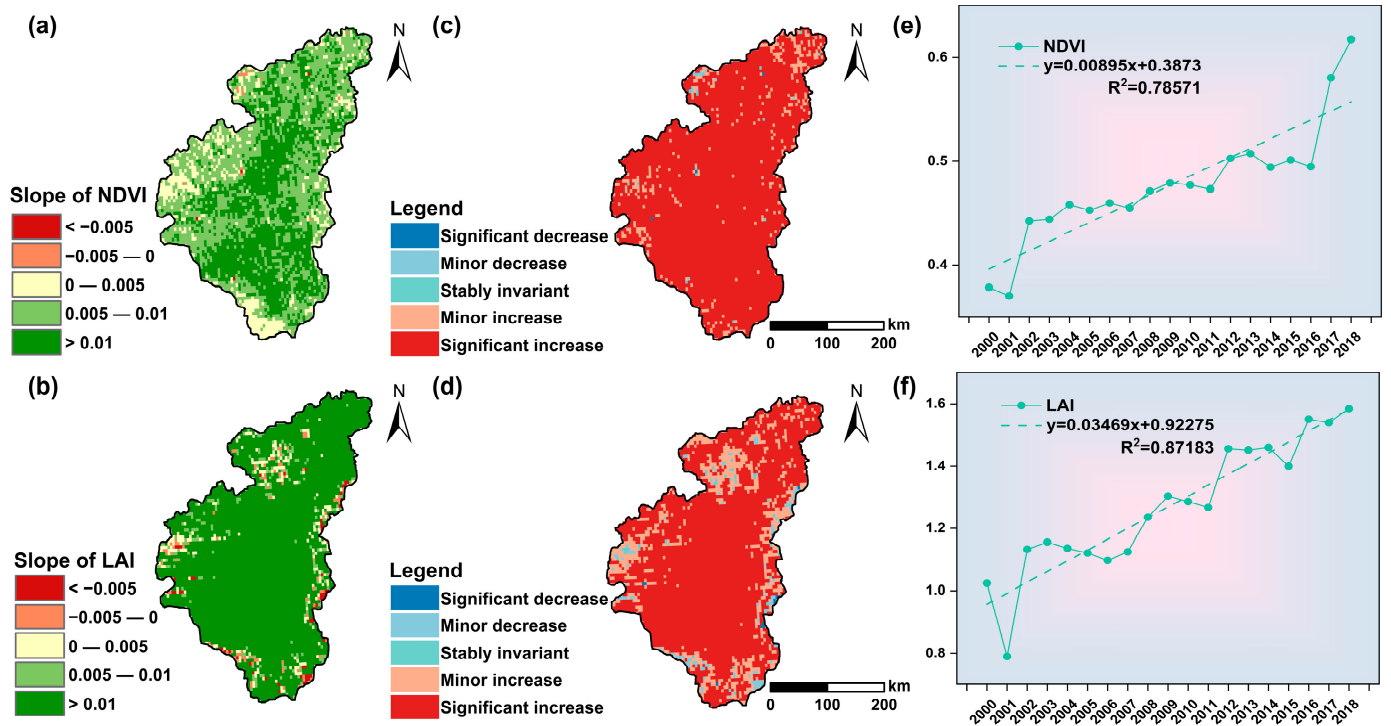
Figure 6. The interannual variation trends in NDVI and LAI in the HLS from 2000 to 2018. (**a**,**b**) The temporal and spatial variation trend in NDVI and LAI from 2000 to 2018. (**c**,**d**) The significance of the changes in NDVI and LAI from 2000 to 2018. (**e**,**f**) The average annual sequence values of NDVI and LAI from 2000 to 2018.

3.3. ET Simulation Results Based on the PT-JPL Model

Figure 7 shows the trend slope and significance test results for the actual ET, Et, Es, and Ei in the HLS from 2000 to 2018 based on the PT-JPL model simulation under the actual vegetation restoration scenario. It can be seen that ET, Es, and Ei showed different degrees of an increasing trend (Figure 6a–d) in 2000–2018, except for the decreasing trend in Et in the HLS. Among them, ET showed an increasing trend in the northern and central regions of the HLS (72.4%), while the southern and northeastern regions (27.2%) showed a decreasing trend (Figure 7e). Regarding Et, 80.4% showed a decreasing trend, and a few areas in the central region showed an increasing trend (Figure 7f). Ei exhibited a rising trend in the northern region of the HLS and a notably declining trend in the southern region, while the central region experienced a significant upward trend in most areas (Figure 7g). Meanwhile, Es showed a marked increase across the majority of the HLS (83.4%), representing the most substantial growth among the various ET types (Figure 7h).

Under the scenario of vegetation remaining unchanged (Figure 8), different components of ET showed significant spatial heterogeneity. From 2000 to 2018, ET, Et, Es, and Ei in the HLS showed a similar trend; that is, the northern and southern parts of the study area decreased, and the central part increased. Specifically, ET showed an increasing trend in the northern and central regions of the HLS (62.0%), while the southern and northeastern regions (37.7%) showed a decreasing trend (Figure 8e). From 2000 to 2018, the trend of increase or decrease of Et in the HLS was very significant. The area with a significant increase (59.0%) was distributed in the middle, while the north and south showed a significant decrease (37.5%). The variation trend in intercepted evaporation (Ei) in different regions is more complex. The south mainly shows a decrease (34.8%), the middle shows a significant increase and a slight increase (64.8%), and the northern region shows a slight decrease. The increase or decrease in soil evaporation (Es) in most areas of the HLS was not significant. Only the central part showed a significant increase (13.6%), the southern region showed a slight decrease, and the rest showed a slight increase (59.2%).
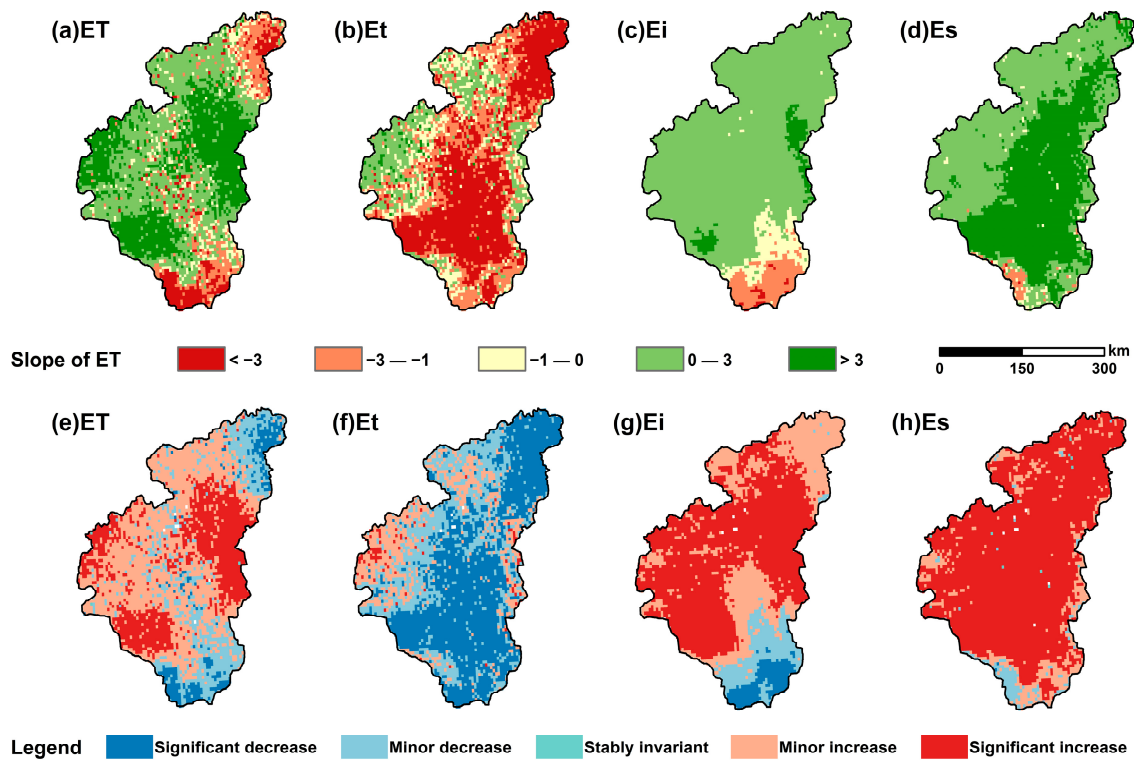
Figure 7. Slope of ET (**a**), Et (**b**), Ei (**c**), and Es (**d**) and the significance test of the slope of ET (**e**), Et (**f**), Ei (**g**), and Es (**h**) in the HLS from 2000 to 2018 under the vegetation change scenario simulated by PT-JPL.
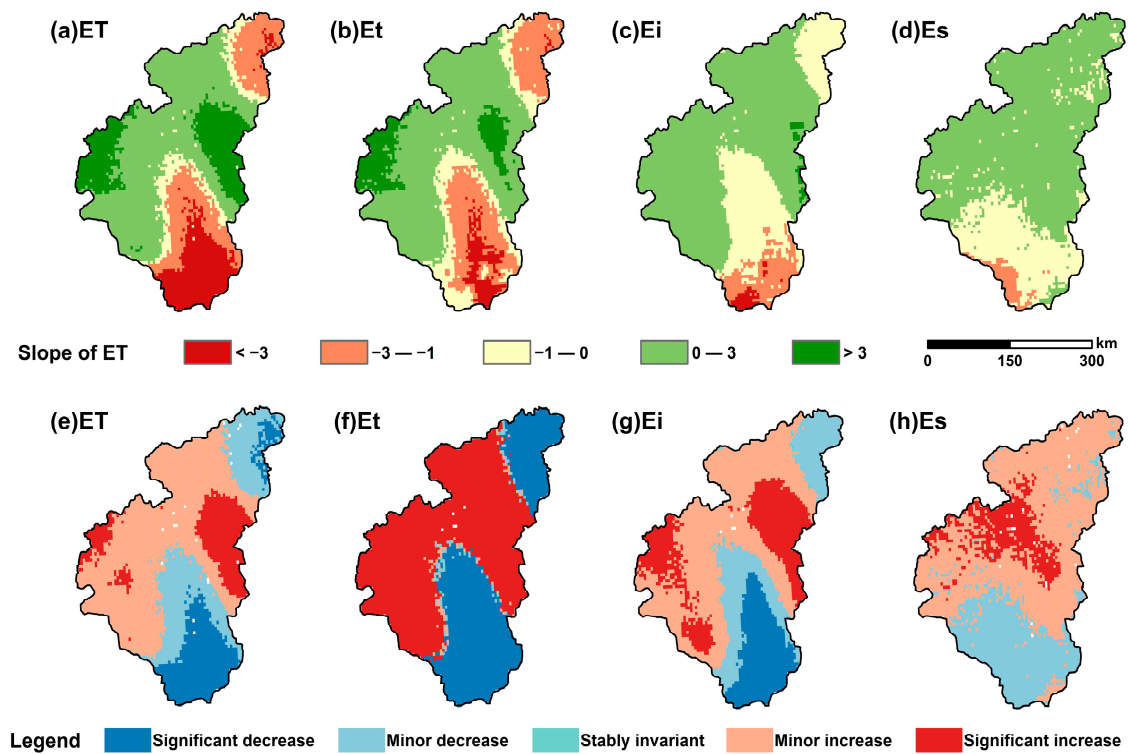

Figure 8. Slope of ET (**a**), Et (**b**), Ei (**c**), and Es (**d**) and the significance test of the slope of ET (**e**), Et (**f**), Ei (**g**), and Es (**h**) in the HLS from 2000 to 2018 under the condition of constant vegetation control simulated by PT-JPL.

3.4. Effects of Vegetation Changes on Evapotranspiration

Figure 9a shows the interannual variation in ET under vegetation-change and no-change scenarios. From 2000 to 2018, the ET in the vegetation-change and no-change scenarios in the HLS showed an overall increasing trend, with an increase rate of 1.33 mm/a and 0.569 mm/a, respectively. Specifically, ET in both cases was at a relatively low level (360 mm) in 2001, 2004–2011, 2015, and 2017. The ET difference between the vegetation change and the vegetation unchanged scenario is in a state of continuous increase (0.75 mm/a) on the whole, with an average annual difference of 3.95 mm, and the maximum difference was 14.51 mm in 2015. In 2000–2003 and 2006, the ET under the vegetation-change scenario was less than the ET under the vegetation-unchanged scenario. From 2000 to 2018, Et under the scenario of vegetation change in the HLS decreased year by year, with a decrease rate of 2.52 mm/a. In contrast, Et under the scenario of unchanged vegetation showed a relatively slow growth trend (0.48 mm/a). The difference between Et in the vegetation-change and vegetation-constant scenario is in a state of continuous decrease (3.00 mm/a), and Et in the vegetation-change scenario is always smaller than Et under the vegetation-constant scenario.
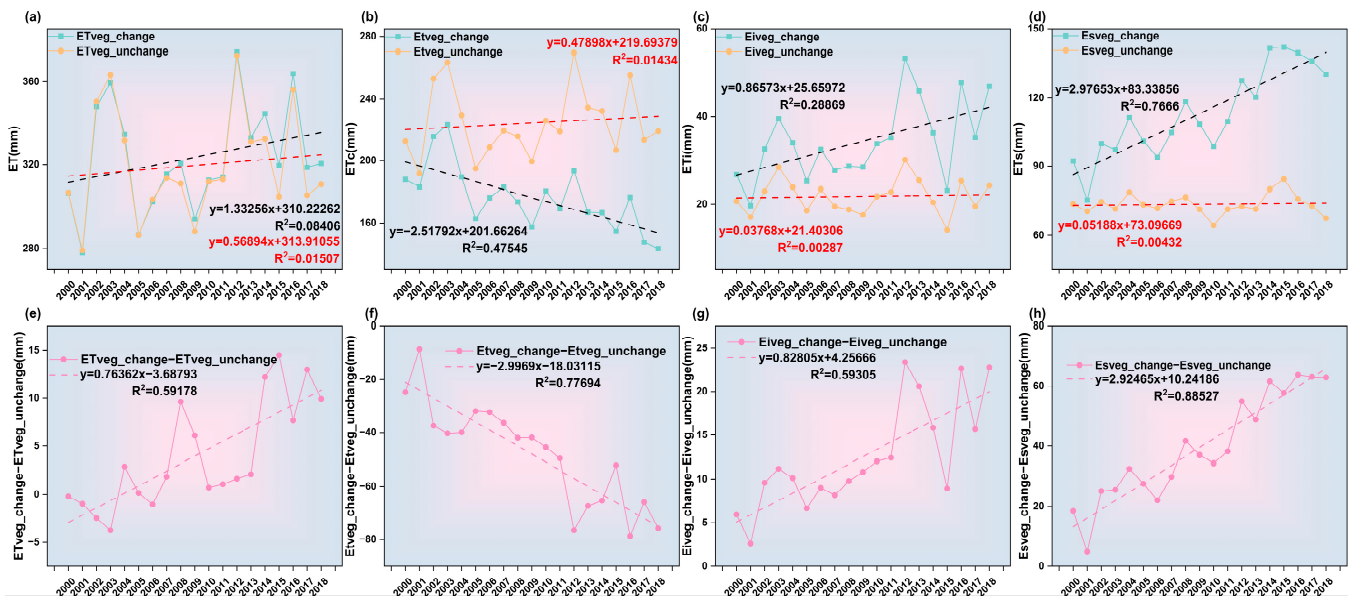

Figure 9. Effect of vegetation greening on the HLS ET. (**a**–**d**) The green line represents the regional mean annual values for actual ET, the orange line represents the regional mean annual values of ET for the vegetation-neutral scenario, and the dashed line represents their trends. (**e**–**h**) Difference between the annual values of ET for the vegetation-variable and vegetation-invariable scenarios, with the dashed line indicating their trends.

Under the scenario of vegetation change, the HLS experienced varying levels of increase in Ei and Es, with growth rates of 0.87 and 2.99 mm/a, respectively. However, from the time series of the two changes, Ei peaked in 2012 and then decreased, while Es remained at a high level after 2012. In the case of constant vegetation, Ei and Es in the HLS did not change much as a whole, and the growth rate was about 0.04 mm/a. During the study period, the Ei difference between the vegetation-change and the vegetation-constant scenario generally showed an increasing state (0.83 mm/a), but the fluctuation was large, especially after 2011. Compared with Ei, the increase state of Es was more stable ($R^2 = 0.88527$), and the increase rate reached 2.92 mm/a.

Figure 10 shows the spatial distribution of the average ET and the difference between them in the HLS simulated by the PT-JPL model in vegetation-change and no-change scenarios. Figure 10a shows that in the vegetation-change scenario, the average ET in the HLS showed a gradual increase from north to south during 2000–2018, showing significant

spatial heterogeneity. In this scenario, the average ET in the southern region of the HLS is higher, reaching 668.5 mm, while ET in the northern and central regions is lower. The reason for this difference is that the land use type in the southern region of the HLS is dominated by forest land. Forest land has high vegetation coverage and strong transpiration, which can significantly increase water vapor transport through canopy interception and transpiration processes, resulting in an ET in the southern forest area of the HLS higher than that in the northern and central grassland areas. Figure 10b illustrates the spatial distribution of average ET in the HLS from 2000 to 2018 under a constant-vegetation scenario. Comparable to the ET variation under the vegetation-change scenario, the multi-year average ET under the vegetation-unchanged scenario exhibited a decreasing trend from south to north. In this scenario, the average ET in the southern region remains higher, though slightly lower than the value under the vegetation change scenario, at 663.8 mm. ET in the northern and central regions also remained low. Figure 10c shows the difference in multi-year average ET between the vegetation-change scenario and no-vegetation-change scenario. The results show that the average ET under the vegetation-change scenario is higher than that under the no-change scenario in most areas, especially in the southern region, and the difference in annual average ET is more than 100 mm. The difference in annual average ET in the central region is between −50 and 50 mm; in some areas of the north, the ET under the vegetation-change scenario is lower than that under the no-change scenario.
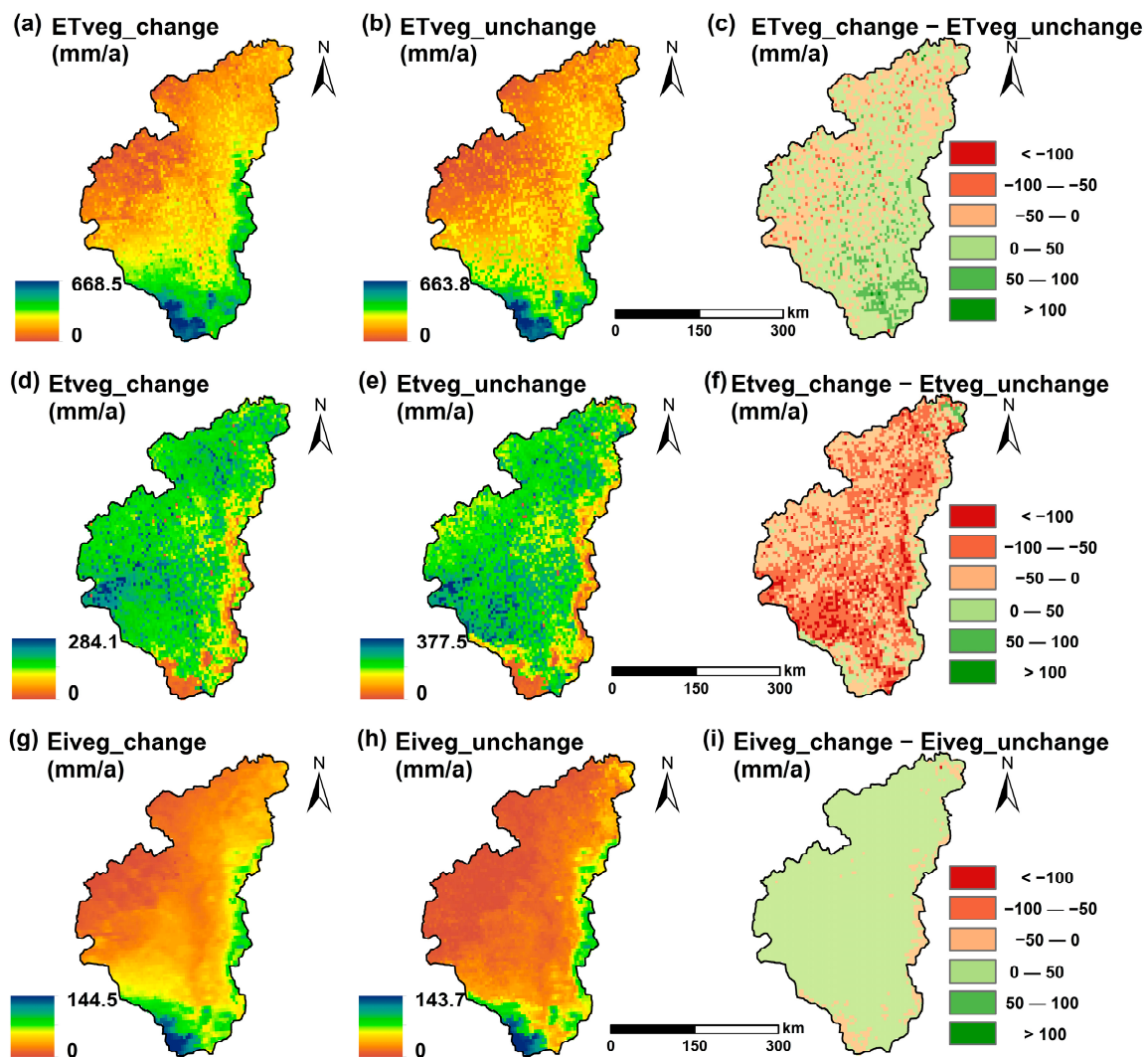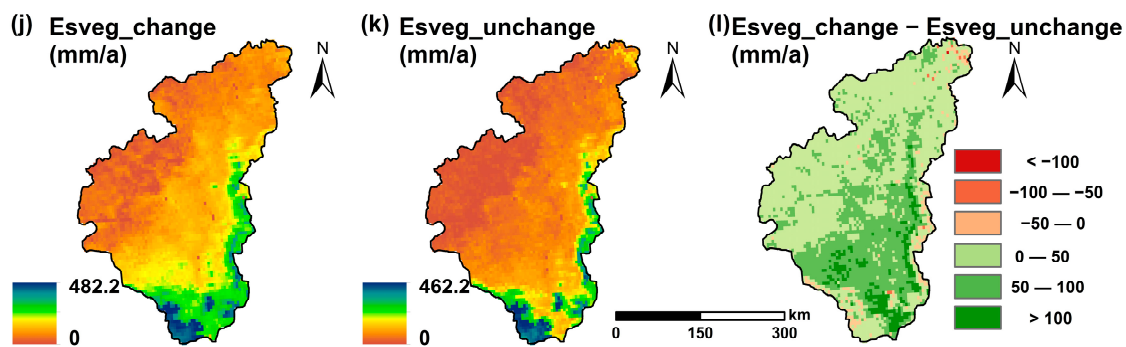

Figure 10. *Cont.*

Figure 10. (**a,b,d,e,g,h,j,k**) The average annual ET (Et, Ei, Es) in the HLS from 2000 to 2018 under the two scenarios. (**c,f,i,l**) The difference between ET and its components in the two situations in the HLS from 2000 to 2018.

3.5. Trends in Climatic Factors and Their Mechanisms of Influence on ET

The change in ET is driven by the change in water supply, atmospheric ET demand, and vegetation physiological characteristics. The initial part of this paper investigates the role of vegetation changes in ET over a 19-year period. Utilizing the multiple regression method, the study examines the effects of climate change on ET in the HLS from 2000 to 2018. Figure 11a shows the spatial distribution of the MK trend change in PRE in the HLS from 2000 to 2018. The results show that the PRE in the HLS shows an increasing trend, and the overall growth rate is greater than 3 mm/a. The growth rate in the central region is greater than that in the southern and northern regions. Figure 11b shows the spatial distribution of the MK trend change in TMP. TMP increased significantly in the northern and central regions of the HLS, while TMP decreased significantly in the southwestern region. Figure 11c shows that the RAD in the northern part of the HLS shows an increasing trend, and the increase rate is greater than 0.3 $W/m^2/a$. The RAD in the southeastern region exhibited a declining trend, with a decrease rate of approximately 0.1 $W/m^2/a$. As shown in Figure 11d, the VPD in the northern part of the HLS decreased at a rate of 0.001–0.003 kPa/a. Conversely, the RAD in the southeastern region demonstrated an increasing trend, with a rate exceeding 0.001 kPa/a. Figure 11e–h illustrate the distribution of significant changes in PRE, TMP, RAD, and VPD. PRE showed a marked increasing trend across most areas of the entire HLS. Significant increases in TMP and RAD were primarily concentrated in the central and northern regions. VPD exhibited a significant decreasing trend across most areas of the HLS. Figure 11i–l depict the trend in changes in PRE, TMP, RAD, and VPD in the HLS from 2000 to 2018. During this period, the annual PRE value increased from 400 mm to approximately 500 mm, indicating a clear upward trend with an average annual increase of 3.57 mm. The annual TMP value increased from about 7.84 °C to about 8.42 °C, with an average annual increase of 0.015 °C. The annual RAD value increased from about 460 W/m^2 to about 475 W/m^2, which also showed a significant upward trend, with an increase rate of 0.20 $W/(m^2 \cdot a)$. The annual VPD value decreased from about 0.45 kPa to about 0.41 kPa, showing a downward trend, with an average annual decrease of 6.43 kPa.
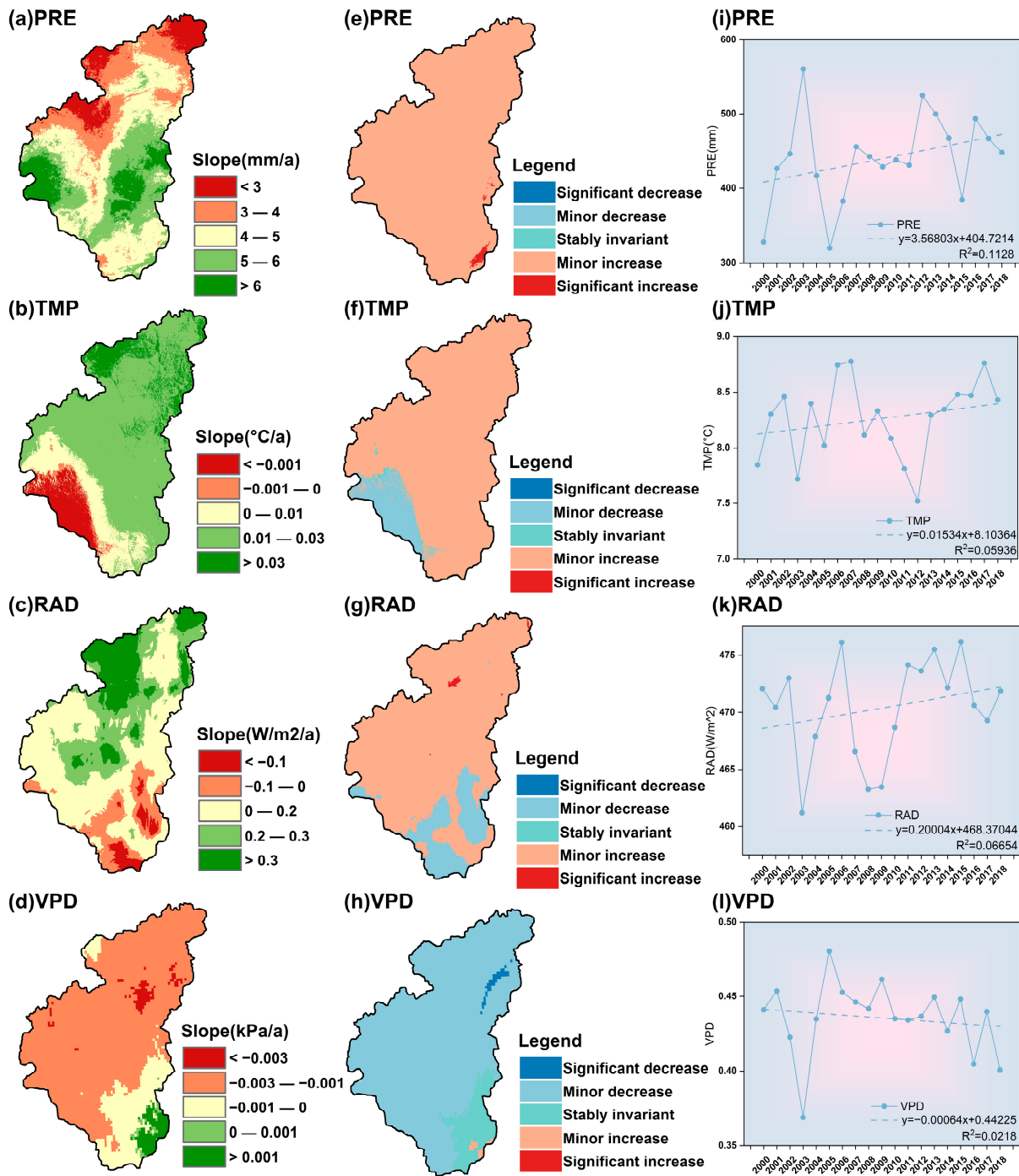
Figure 11. Trend in the annual PRE, TMP, RAD, and VPD in the HLS from 2000 to 2018. (**a**–**d**) Spatial dynamics of PRE, TMP, RAD, and VPD. (**e**–**h**) The significance of the changes in PRE, TMP, RAD, and VPD. (**i**–**l**) Time series of the annual PRE, TMP, RAD, and VPD from 2000 to 2018.

Figure 12 illustrates the spatial distribution of the impact of climatic factors on the variations of ET, Et, Ei, and Es in the HLS from 2000 to 2018. Figure 12a–d depict the influence of PRE, TMP, RAD, and VPD on ET changes. The contribution of PRE (Figure 12a) to ET change is generally positive across most regions, with a contribution rate of 0–0.5 mm/a in the northern and central areas, while it is negative in the southern region (−0.5–0 mm/a). The contribution of TMP (Figure 12b) to ET is more significant, and the central and southern regions show mainly negative contributions (−3–1 mm/a), while some northern and western regions show positive contributions. The RAD (Figure 12c) mainly showed a

positive contribution to ET, and the contribution rate in the central region was about 0.5–3 mm/a, while the southern and northern regions showed a negative contribution (−0.5–3 mm/a). The VPD (Figure 12d) in the HLS showed a strong negative contribution to ET, and the negative contribution rate in most areas exceeded 3 mm/a. Figure 12e–h show the contribution of different climatic factors to Et changes. The contribution of PRE (Figure 12e) to Et is mainly positive, concentrated in the northern and central regions, and the PRE in the southern region shows a negative contribution to Et. The effect of TMP (Figure 12f) on Et showed a negative contribution in the central and southern regions and a positive contribution in some northern regions. The contribution of the RAD (Figure 12g) to Et is more dispersed, showing a mixed distribution of regional positive and negative contributions. The contribution of VPD (Figure 12h) to Et is negative in most areas of the study area, especially in the southern and central regions, but the positive contribution of VPD to Et in some parts of the central region is very significant (>3 mm/a). Figure 12i–l show the contribution of different climatic factors to the change in Ei. The contribution of PRE (Figure 12i) to Ei is positive in most regions. The contribution of TMP (Figure 12j) to Ei is positive in the northern region and some central regions, while the southern region shows a negative contribution. The contribution of the RAD (Figure 11k) to Ei is small, with most areas ranging from −0.5 to 0.5 mm/a. The contribution of VPD (Figure 12l) to Ei is mostly negative in the study area, especially in the southern region. Figure 12m–p shows the contribution of different climatic factors to Es changes. The contribution of PRE (Figure 12m) to Es is positive in most regions, but the overall contribution is small. The contribution of TMP (Figure 12n) to Es showed a positive and negative mixed spatial pattern, mainly concentrated in the northern and central positive contribution areas. The contribution of the RAD (Figure 12o) to Es is small in most regions, ranging from −0.5 to 0.5 mm/a. The contribution of VPD (Figure 12p) to Es is mostly negative in the study area, especially in the southern region, showing a significant negative contribution.

In order to study the ET and its driving mechanism in the Helong region more clearly, we also analyzed the dominant factors of ET, Et, Ei, and Es under four climate impact factors (PRE, TMP, RAD, and VPD) and vegetation change scenarios simulated by the PT-JPL model. The results of the dominant factor analysis of ET showed that TMP was the main factor affecting its change, accounting for 37.2%. The areas dominated by VPD, PRE, and RAD accounted for 21.9%, 30.5%, and 10.4%, respectively (Figure 13a). For Et, the dominant influence factor is VPD, and its dominant influence area accounts for 67.8%. Compared with ET, the dominant influence area of VPD is significantly increased. For Ei, the dominant influence area of TMP and RAD increased to 37.8% and 40.1%, respectively, and only the dominant influence area of PRE remained stable at a low level of 0.3%. For Es, the dominant influence area of TMP continued to increase, while the dominant influence area of RAD and VPD continued to decrease, reaching 11.8% and 33.8%, respectively, and the dominant influence area of PRE remained at a level of 0.3%. From a distribution point of view, the dominant influence area of TMP is distributed in all regions except the northern and northeastern edges; the dominant influence areas of PRE are mainly distributed in the north and west; the dominant influence area of RAD is distributed in the western region; and the dominant influence areas of VPD are scattered throughout the HLS. TMP had significant effects on ET, Et, Ei, and Es, especially in the central and southern regions. PRE mainly played a leading role in the northern and western regions. RAD had a greater impact on the west, while VPD had a relatively scattered impact on the components of ET.

The GOF indices of the structural models constructed by ET, Et, Ei, and Es are 0.58, 0.53, 0.57, and 0.43, respectively (Figure 14). Therefore, from a mathematical point of view, the model that we constructed is feasible. The overall explanation rate of driving factors for ET is more than 68.9%, the overall explanation rate for Et is more than 73.4%, the overall explanation rate for Ei is more than 62.5%, and the overall explanation rate for Es is 7.8%, which is at a low level. Please refer to Table 4 for the specific path coefficient values. Among them, the path coefficients of Es and various driving factors change greatly. The path coefficient of PRE changes from positive to negative compared with other factors.

The influence of VPD and RAD on it is greatly reduced compared with other factors. The path coefficient of TMP changes from negative to positive compared with other factors. In addition, in the relationship between driving factors, the path coefficient of PRE to VPD is −0.654, which is at a high level. The path coefficient of LAI to PRE is 0.432, and the path coefficients of PRE and LAI to TMP are −0.22 and 0.198, respectively. The path coefficient of RAD to TMP is 0.016.
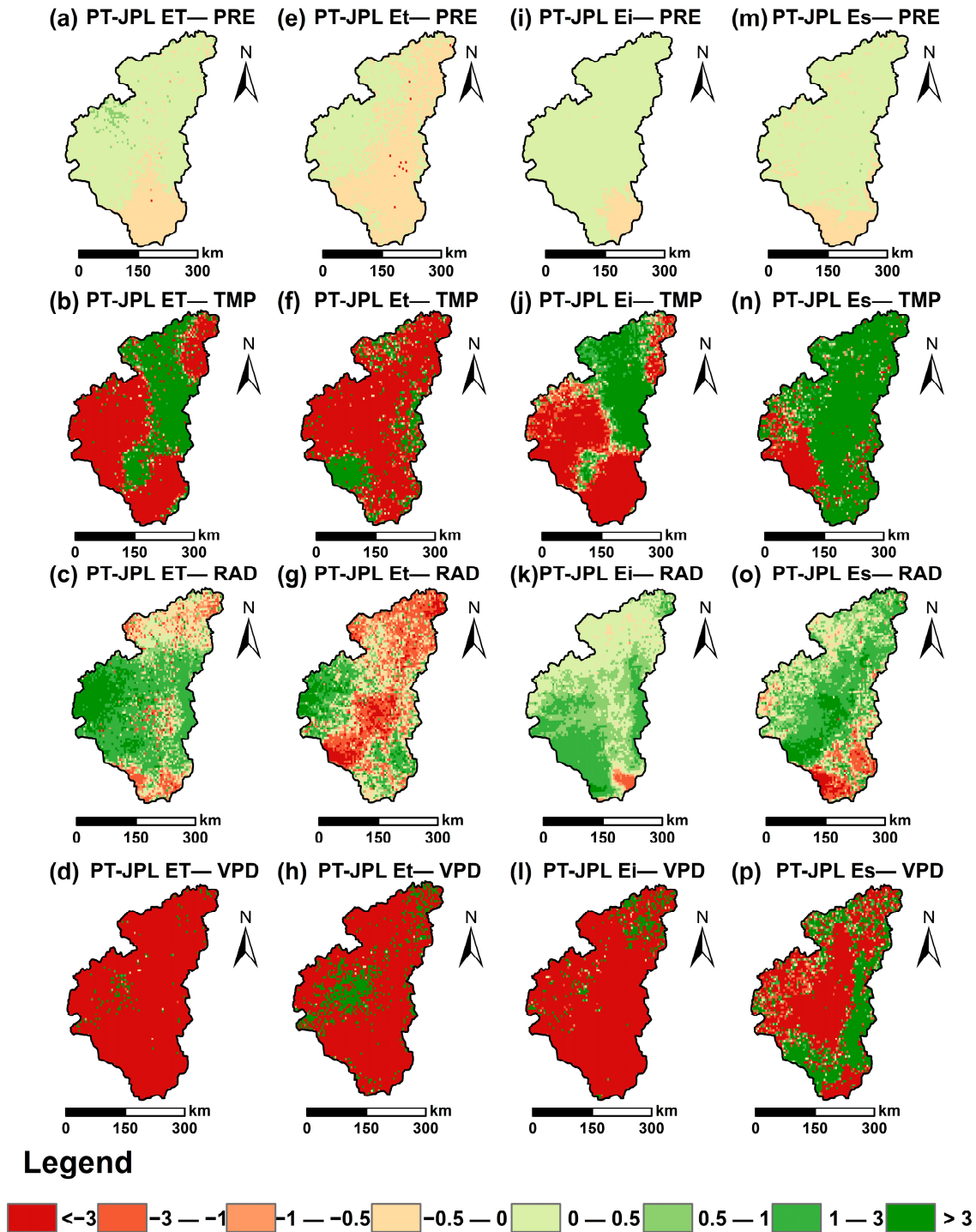

Figure 12. The spatial pattern of the influence/contributions of four climate factors (PRE, TMP, RAD, and VPD) on PT-JPL ET change under MLR, ET (**a–d**), Et (**e–h**), Ei (**i–l**), and Es (**m–p**).
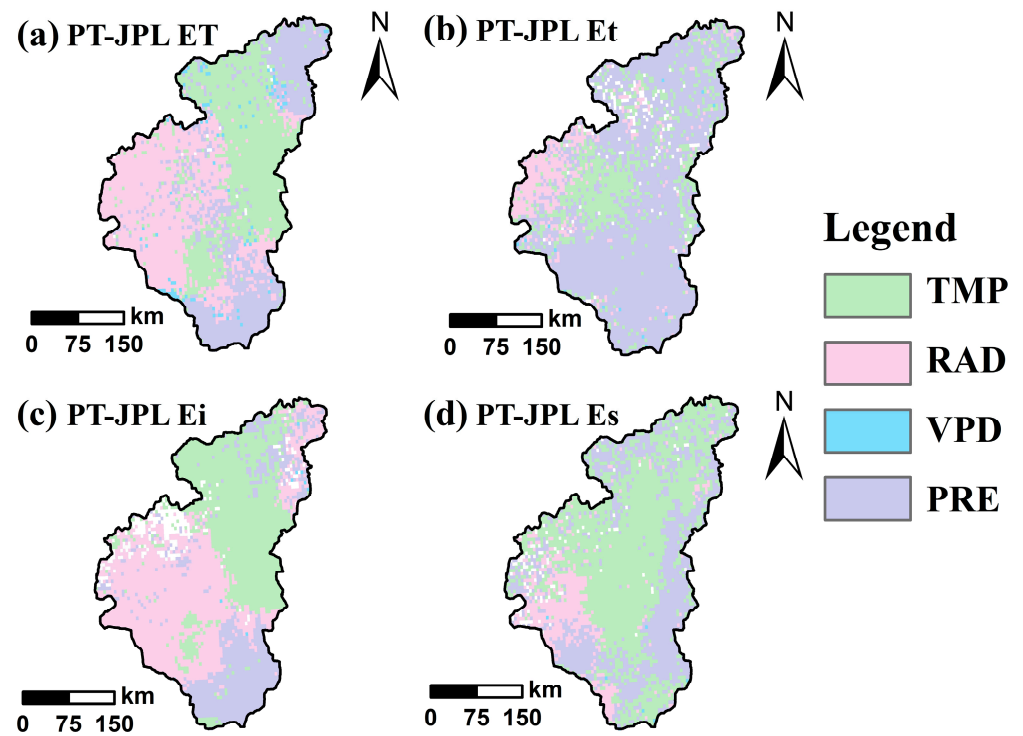
Figure 13. (**a**) Spatial patterns of ET's dominant factors. (**b**) Spatial patterns of Et's dominant factors. (**c**) Spatial patterns of Ei's dominant factors. (**d**) Spatial patterns of Es's dominant factors.
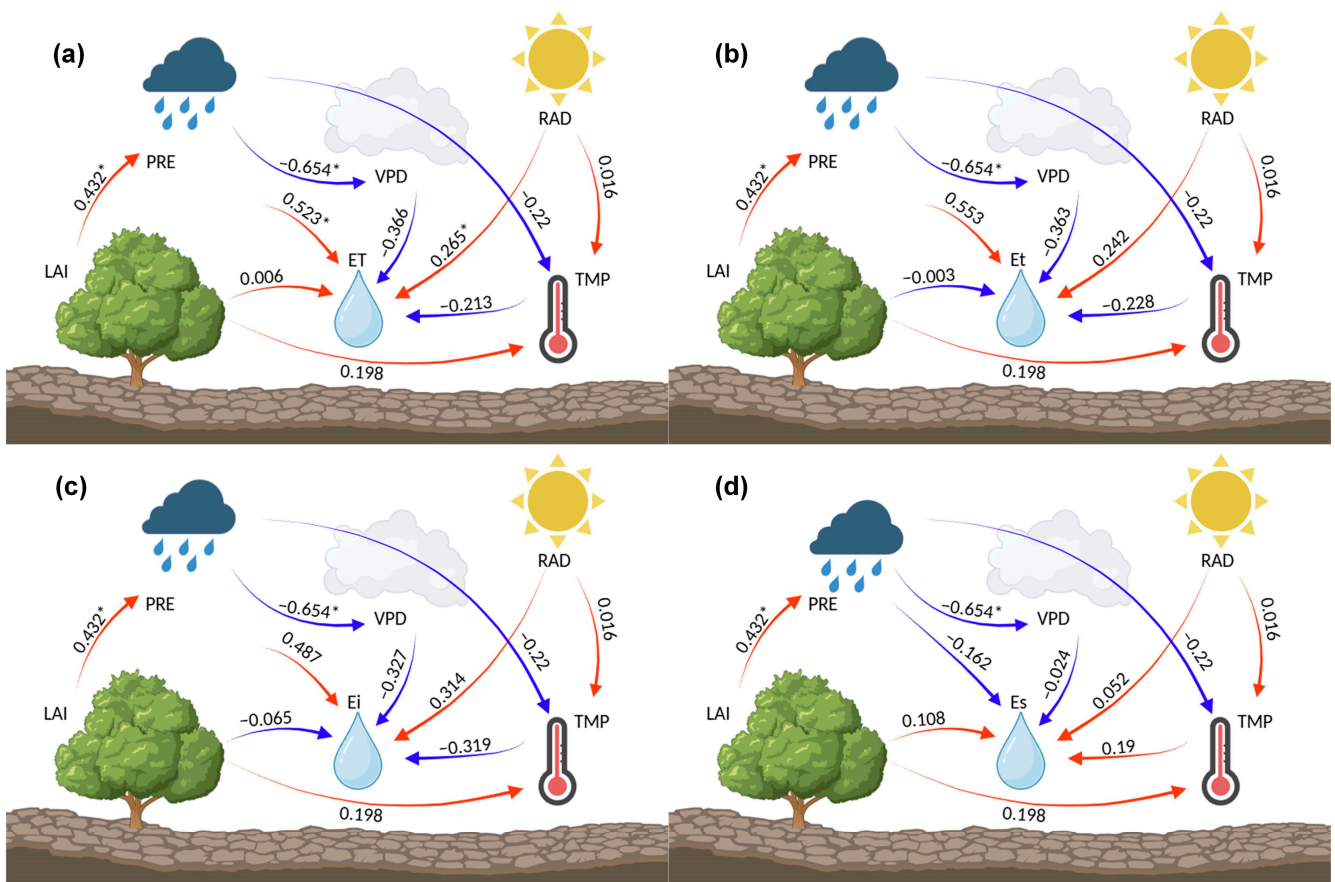

Figure 14. Analysis of direct and indirect effects of climate and vegetation conditions on (**a**) ET, (**b**) Et, (**c**) Ei, (**d**) Es. * $p < 0.05$.

Table 4. The path coefficient of LAI, PRE, TMP, RAD, and VPD on the changes in ET, Et, Ei, and Es based on the PLS-SEM model.

Pathway	PRE	RAD	TMP	VPD	ET	Et	Ei	Es
LAI→	0.432 *	0.173	0.198	−0.008	0.006	−0.003	−0.065	0.108
PRE→		−0.22		−0.654 *	0.523 *	0.553 *	0.487 *	−0.162
RAD→			0.016		0.265	0.242	0.314	0.052
TMP→					−0.213	−0.228	−0.319	0.19
VPD→					−0.366	−0.363	−0.327	−0.024

Note: * $p < 0.05$. →: The path coefficient starting from the left factor, LAI→: The path coefficient starting from LAI.

4. Discussion

4.1. Simulation Results and Spatiotemporal Variations in ET, Et, Ei, and Es

In this research, the PT-JPL model was applied to simulate ET, Et, Ei, and Es in the HLS from 2000 to 2018. The validation results indicate that the PT-JPL model effectively simulates the ET process in the HLS, demonstrating a strong correlation with MODIS products and high accuracy. The simulation results revealed that ET, Es, and Ei exhibited an increasing trend during the study period, while Et displayed a decreasing trend. In a study in the same direction, ref. [15] used the generalized complementary relationship to quantitatively analyze the impact of climate change and vegetation restoration on the increase in ET in the Loess Plateau by establishing the relationship between AC and climatic vegetation factors in 14 watersheds of the Loess Plateau from 1981 to 2014. The results indicated that the average annual ET across the 14 watersheds of the Loess Plateau ranged from 300 to 600 mm, with a consistent upward trend observed each year. Work [13] used the ETWatch model to estimate the actual evapotranspiration (ET) in China's Loess Plateau from 2000 to 2020 and employed the generalized additive model to quantitatively assess the contributions of climate factors and human activities to ET changes. The results showed that the ET increased from 386.67 mm in 2000 to 544.73 mm in 2020, and the impact of LUCC on ET in the Loess Plateau was greater than that of climate change on ET. Bai et al. [42] simulated the actual ET of the Yanhe River Basin in the typical hilly and gully region of the Loess Plateau from 2000 to 2016 by using the VIP model based on remote sensing. The actual ET was 324–529 mm, and the ET continued to increase over the 17 years. These results are consistent with our simulation results, indicating that our PT-JPL model is reliable and applicable in capturing the dynamic changes in evapotranspiration in the HLS.

4.2. Effects of Vegetation and Climate Change on ET in the HLS

Following the simulation and validation of ET, we further investigated the effects of climate change on ET and its components within the HLS. When analyzing the influence of climate factors on ET, we observed that temperature (TMP) had a more pronounced impact, exhibiting a negative contribution in the central and southern regions, while contributing positively in the northern and western regions. High temperature intensifies transpiration and soil evaporation, but may also lead to soil drying, which limits further ET [43]. In the central and southern regions, persistent high temperatures can cause the rapid evaporation of soil moisture, preventing vegetation roots from absorbing water promptly, which leads to water deficits in plants and weakens transpiration, ultimately reducing the overall ET [8]. In the northern and western regions, a moderate increase in temperature may contribute to an increase in plant growth and ET, especially in the relatively low-temperature season. A moderate temperature increase can promote the photosynthesis and growth of plants and enhance transpiration. The contribution of radiation (RAD) to ET was mainly positive, with a higher contribution rate in the central region, while the southern and northern regions showed a negative contribution. The higher radiation in the central region promoted photosynthesis and transpiration, thus increasing ET [44]. Increased radiation usually increases leaf temperature and photosynthetic efficiency and increases the transpiration rate of water through the stomata. Therefore, in the central region with sufficient light, the increase in radiation significantly increased ET. The negative contribution of the southern

and northern parts may be due to the reduction in vegetation damage and ET caused by excessive radiation. Excessive radiation may lead to photoinhibition in plants, reduce the efficiency of photosynthesis, and even cause leaf burns, damage plant health, and reduce ET [45]. The negative contribution of VPD to ET was significant in most regions, especially in the southern region. An increase in VPD usually enhances ET demand, but if soil moisture is insufficient, it may limit the actual occurrence of ET [46]. High VPD means high air dryness and enhanced transpiration in plants. However, if the soil moisture is insufficient, then the plant's roots cannot provide sufficient water, and transpiration will be limited. Therefore, in the southern region, although VPD is high, it leads to a decrease in ET due to insufficient soil water supply. The positive contribution of PRE to ET was mainly concentrated in the northern and central regions, while the southern region showed a negative contribution. This phenomenon may be related to the soil type and vegetation type in the region, which may limit the positive effect of PRE on ET. For example, the soil types in the northern and central regions are relatively loose, which can better store and utilize PRE, promote vegetation growth, and increase ET, while the soil in the southern region may be denser, which limits the infiltration and storage of water, resulting in a lower contribution of PRE to ET [47]. For Et, VPD is the main influencing factor, especially in the central and southern regions. The contribution of TMP and PRE to Et showed significant spatial heterogeneity. TMP had a significant negative contribution to Et in the central and southern regions, while PRE had a positive contribution to Et in the northern and central regions. The contribution of RAD to Et was more dispersed, showing a mixed distribution of positive and negative contributions. This phenomenon may be related to vegetation type and coverage, and the response of vegetation to climate factors is different in different regions [6]. For example, dense woodlands may have a stronger response to precipitation and radiation, while loose grasslands are more sensitive to temperature changes. The dominant influence area of Ei, TMP, and RAD increased significantly, while the dominant influence area of PRE was smaller. The contribution of TMP to Ei is positive in the north and part of the central region, while the southern region shows a negative contribution. The contribution of RAD to Ei is small, ranging from −0.5 to 0.5 mm/a in most areas. The contribution of VPD to Ei is negative in most regions, especially in the southern region. This may be due to the fact that Ei is mainly affected by leaf area index and precipitation, while TMP and RAD have a greater impact on these factors [48]. Under conditions of high temperature and radiation, leaf water evaporation increased, leading to a rise in Ei. For Es, the area primarily influenced by TMP expanded, while the areas influenced by RAD and VPD contracted. TMP's contribution to Es was more pronounced in the northern and central regions. The contribution of RAD to Es was small in most regions, about −0.5 to 0.5 mm/a. The contribution of VPD to Es was mostly negative in the study area, especially in the southern region, showing a significant negative contribution. This may be closely related to soil type and water status, and the response of soil in different regions to climatic factors is different [49]. For example, sandy soil has a weak water retention capacity, and soil moisture is easily lost under high-temperature and high-VPD conditions, resulting in a decrease in Es.

4.3. Inspiration and Suggestions for Water Resources and Vegetation Protection and Greening

Through a comprehensive analysis of climate factors and vegetation changes, our study reveals the complexity of the ET process in the HLS. These results have important implications for regional water resources management and vegetation restoration. First of all, differentiated water resource management strategies should be formulated according to the climatic characteristics and vegetation types of different regions. For example, in the northern and central regions with high precipitation, vegetation restoration projects can be appropriately increased to improve ET and water cycle efficiency; in the southern region, soil moisture management should be a focus, to alleviate the adverse effects of high temperature and water vapor pressure deficit on ET [50]. Secondly, it is crucial to enhance the monitoring and forecasting of climate change, with particular emphasis on the

long-term tracking of key factors such as temperature, radiation, and water vapor pressure deficit [51]. This will help us to foresee the potential impacts of climate change on regional water resources and ecosystems and to take appropriate response measures.

4.4. Uncertainties and Limitations

While this study has revealed significant insights into the effects of climatic factors and vegetation restoration on ET and its components in the HLS, certain uncertainties and limitations remain. Firstly, the parameter settings of the PT-JPL model and the quality of input data could influence the simulation results. Future research should focus on further optimizing the model parameters and employing higher-resolution observational data for validation [52]. Secondly, this study focuses on the effects of climate factors and vegetation restoration on ET, while the effects of other potential factors (human activities) on ET have not been fully considered. Future research should comprehensively consider the combined effects of multiple factors to understand the driving mechanism of ET more comprehensively [53]. Finally, the time scale of this study is 2000–2018, and the time span is relatively short. Future research should consider climate change and vegetation dynamics on a longer time scale in order to better predict future trends.

5. Conclusions

The PT-JPL model was used to simulate ET and its components in the HLS, and the impact of vegetation restoration and climate change on ET were explored. The main conclusions are as follows:

(1) During 2000–2018, the ET, Ei, and Es of the HLS increased at a rate of 1.33, 0.87, and 2.99 mm/a, respectively, and the Et decreased at a rate of 2.52 mm/a under the vegetation-change scenario. The ET, Et, Ei, and Es increased at a rate of 0.57, 0.47, 0.04, and 0.04 mm/a, respectively.

(2) Vegetation restoration led to a significant increase in the evaporation water consumption of the HLS. Vegetation restoration increased the annual ET from 331.26 mm (vegetation-unchanged scenario) to 338.85 mm (vegetation-change scenario), an increase of 2.3% from 2000 to 2018. The change rates in ET, Et, Ei, and Es directly caused by vegetation change were 0.76, −1.95, 0.83, and 2.95 mm/a, respectively.

(3) PRE made a positive contribution to ET primarily in the northern and central regions. TMP showed a negative contribution in the central and southern regions. The high value of VPD is mainly concentrated in the southern region, which has a significant negative contribution to ET. TMP was the main factor affecting its change, and the dominant influence area accounted for 37.2%. PRE and VPD were identified as the main factors affecting ET changes.

Author Contributions: P.H.: conceptualization, methodology, software, formal analysis, writing—original draft. G.Y.: conceptualization, modifying figures. Y.L.: conceptualization, methodology, project administration, funding acquisition, supervision. X.C.: data curation. Z.W.: data curation. H.S.: data curation. E.H.: data curation. T.X.: data curation. Y.Z.: data curation. All authors have read and agreed to the published version of the manuscript.

Data Availability Statement: Data are contained within the article.

Conflicts of Interest: The authors declare that they have no known competing financial interests or personal relationships that could have appeared to influence the work reported in this paper.

References

1. Zanin, P.R.; Pareja-Quispe, D.; Espinoza, J.-C. Evapotranspiration in the Amazon Basin: Couplings, hydrological memory and water feedback. *Agric. For. Meteorol.* **2024**, *352*, 110040. [CrossRef]
2. Liu, J.; You, Y.; Li, J.; Sitch, S.; Gu, X.; Nabel, J.E.M.S.; Lombardozzi, D.; Luo, M.; Feng, X.; Arneth, A.; et al. Response of global land evapotranspiration to climate change, elevated CO2, and land use change. *Agric. For. Meteorol.* **2021**, *311*, 108663. [CrossRef]
3. Forster, M.A.; Kim, T.D.H.; Kunz, S.; Abuseif, M.; Chulliparambil, V.R.; Srichandra, J.; Michael, R.N. Phenology and canopy conductance limit the accuracy of 20 evapotranspiration models in predicting transpiration. *Agric. For. Meteorol.* **2022**, *315*, 108824. [CrossRef]
4. Zhao, J.; Yang, J.; Huang, R.; Xie, H.; Qin, X.; Hu, Y. Estimating evapotranspiration and drought dynamics of winter wheat under climate change: A case study in Huang-Huai-Hai region, China. *Sci. Total Environ.* **2024**, *949*, 175114. [CrossRef]
5. Wang, C.; Chen, J.; Gu, L.; Wu, G.; Tong, S.; Xiong, L.; Xu, C.-Y. A pathway analysis method for quantifying the contributions of precipitation and potential evapotranspiration anomalies to soil moisture drought. *J. Hydrol.* **2023**, *621*, 129570. [CrossRef]
6. Perez, M.; Lombardi, D.; Bardino, G.; Vitale, M. Drought assessment through actual evapotranspiration in Mediterranean vegetation dynamics. *Ecol. Indic.* **2024**, *166*, 112359. [CrossRef]
7. Zhu, W.; Fan, L.; Jia, S. Integration of microwave satellite soil moisture products in the contextual surface temperature-vegetation index models for spatially continuous evapotranspiration estimation. *ISPRS J. Photogramm. Remote Sens.* **2023**, *203*, 211–229. [CrossRef]
8. Yu, Z.; Chen, J.; Chen, J.; Zhan, W.; Wang, C.; Ma, W.; Yao, X.; Zhou, S.; Zhu, K.; Sun, R. Enhanced observations from an optimized soil-canopy-photosynthesis and energy flux model revealed evapotranspiration-shading cooling dynamics of urban vegetation during extreme heat. *Remote Sens. Environ.* **2024**, *305*, 114098. [CrossRef]
9. Wang, Z.; Li, J.; Hou, J.; Zhao, K.; Wu, R.; Sun, B.; Lu, J.; Liu, Y.; Cui, C.; Liu, J. Enhanced evapotranspiration induced by vegetation restoration may pose water resource risks under climate change in the Yellow River Basin. *Ecol. Indic.* **2024**, *162*, 112060. [CrossRef]
10. Ji, Z.; Wang, Y.; Wang, L. Threshold identification of evapotranspiration under different land-use types in the Loess Plateau, China. *J. Hydrol. Reg. Stud.* **2024**, *53*, 101780. [CrossRef]
11. Liu, Y.; Lin, Z.; Wang, Z.; Chen, X.; Han, P.; Wang, B.; Wang, Z.; Wen, Z.; Shi, H.; Zhang, Z.; et al. Discriminating the impacts of vegetation greening and climate change on the changes in evapotranspiration and transpiration fraction over the Yellow River Basin. *Sci. Total Environ.* **2023**, *904*, 166926. [CrossRef] [PubMed]
12. Martín, J.; Sáez, J.A.; Corchado, E. Tackling the problem of noisy IoT sensor data in smart agriculture: Regression noise filters for enhanced evapotranspiration prediction. *Expert Syst. Appl.* **2024**, *237*, 121608. [CrossRef]
13. Cao, X.; Zheng, Y.; Lei, Q.; Li, W.; Song, S.; Wang, C.; Liu, Y.; Khan, K. Increasing actual evapotranspiration on the Loess Plateau of China: An insight from anthropologic activities and climate change. *Ecol. Indic.* **2023**, *157*, 111235. [CrossRef]
14. Ma, Z.; Yan, N.; Wu, B.; Stein, A.; Zhu, W.; Zeng, H. Variation in actual evapotranspiration following changes in climate and vegetation cover during an ecological restoration period (2000–2015) in the Loess Plateau, China. *Sci. Total Environ.* **2019**, *689*, 534–545. [CrossRef]
15. Li, T.; Xia, J.; Zhang, L.; She, D.; Wang, G.; Cheng, L. An improved complementary relationship for estimating evapotranspiration attributed to climate change and revegetation in the Loess Plateau, China. *J. Hydrol.* **2021**, *592*, 125516. [CrossRef]
16. Lv, X.; Zuo, Z.; Sun, J.; Ni, Y.; Wang, Z. Climatic and human-related indicators and their implications for evapotranspiration management in a watershed of Loess Plateau, China. *Ecol. Indic.* **2019**, *101*, 143–149. [CrossRef]
17. Lin, Z.; Long, T.; Jiao, W.; Ye, Z.; Zhang, D.; He, G. Estimation and spatiotemporal analysis of actual evapotranspiration over Qinghai-Tibet Plateau using an Alpine Grassland-Adapted Priestley-Taylor model. *J. Hydrol.* **2024**, *641*, 131756. [CrossRef]
18. Fisher, J.B.; Tu, K.P.; Baldocchi, D.D. Global estimates of the land–atmosphere water flux based on monthly AVHRR and ISLSCP-II data, validated at 16 FLUXNET sites. *Remote Sens. Environ.* **2008**, *112*, 901–919. [CrossRef]
19. Jiang, X.; Wang, Y.; A., Y.; Wang, G.; Zhang, X.; Ma, G.; Duan, L.; Liu, K. Optimizing actual evapotranspiration simulation to identify evapotranspiration partitioning variations: A fusion of physical processes and machine learning techniques. *Agric. Water Manag.* **2024**, *295*, 108755. [CrossRef]
20. Irmak, S. Maize response to different subsurface drip irrigation management strategies: Yield, production functions, basal and crop evapotranspiration. *Agric. Water Manag.* **2024**, *300*, 108927. [CrossRef]
21. Wang, J.; Gao, X.; Zhao, J.; Ding, Y.; Yang, H.; Zhang, S.; Xueping, Z.; Zhao, X. Evaluation of vegetation–water mutual suitability in Helong Region of the Loess Plateau. *Agric. Water Manag.* **2023**, *290*, 108603. [CrossRef]
22. Yadav, D.; Singh, D.; Babu, S.; Madegowda, M.; Singh, D.; Mandal, D.; Rathore, A.C.; Sharma, V.K.; Singhal, V.; Kumawat, A.; et al. Intensified cropping reduces soil erosion and improves rainfall partitioning and soil properties in the marginal land of the Indian Himalayas. *Int. Soil Water Conserv. Res.* **2024**, *12*, 521–533. [CrossRef]
23. Sun, Y.; Sun, Z.; Zhang, Y.; Qiao, Q. How can governments and fishermen collaborate to participate in a fishing ban for ecological restoration? *J. Environ. Manag.* **2024**, *360*, 120958. [CrossRef]

24. Gao, P.; Deng, J.; Chai, X.; Mu, X.; Zhao, G.; Shao, H.; Sun, W. Dynamic sediment discharge in the Hekou–Longmen region of Yellow River and soil and water conservation implications. *Sci. Total Environ.* **2017**, *578*, 56–66. [CrossRef]

25. Niu, Z.; He, H.; Zhu, G.; Ren, X.; Zhang, L.; Zhang, K.; Yu, G.; Ge, R.; Li, P.; Zeng, N.; et al. An increasing trend in the ratio of transpiration to total terrestrial evapotranspiration in China from 1982 to 2015 caused by greening and warming. *Agric. For. Meteorol.* **2019**, *279*, 107701. [CrossRef]

26. Shao, R.; Zhang, B.; Su, T.; Long, B.; Cheng, L.; Xue, Y.; Yang, W. Estimating the Increase in Regional Evaporative Water Consumption as a Result of Vegetation Restoration Over the Loess Plateau, China. *J. Geophys. Res. Atmos.* **2019**, *124*, 11783–11802. [CrossRef]

27. Allen, R.G. Crop evapotranspiration: Guidelines for computing crop water requirements. *FAO Irrig. Drain.* **1998**, *56*, 147–151.

28. Esri. *ArcGIS Desktop: Release 10.8*; Environmental Systems Research Institute: Redlands, CA, USA, 2020.

29. Shao, R.; Wang, Y.; Shao, W.; Ni, G. Assessing the synergistic modulation of evapotranspiration by global impervious surface and vegetation changes. *Agric. For. Meteorol.* **2022**, *327*, 109194. [CrossRef]

30. Huete, A.; Didan, K.; Miura, T.; Rodriguez, E.P.; Gao, X.; Ferreira, L.G. Overview of the radiometric and biophysical performance of the MODIS vegetation indices. *Remote Sens. Environ.* **2002**, *83*, 195–213. [CrossRef]

31. Yao, N.; Ye, J.; Wang, S.; Yang, S.; Lu, Y.; Zhang, H.; Yang, X. Bias correction of the hourly satellite precipitation product using machine learning methods enhanced with high-resolution WRF meteorological simulations. *Atmos. Res.* **2024**, *310*, 107637. [CrossRef]

32. Zhang, L.; Marshall, M.; Nelson, A.; Vrieling, A. A global assessment of PT-JPL soil evaporation in agroecosystems with optical, thermal, and microwave satellite data. *Agric. For. Meteorol.* **2021**, *306*, 108455. [CrossRef]

33. Ćalasan, M.; Abdel Aleem, S.H.E.; Zobaa, A.F. On the root mean square error (RMSE) calculation for parameter estimation of photovoltaic models: A novel exact analytical solution based on Lambert W function. *Energy Convers. Manag.* **2020**, *210*, 112716. [CrossRef]

34. Han, P.; Yang, G.; Wang, Z.; Liu, Y.; Chen, X.; Zhang, W.; Zhang, Z.; Wen, Z.; Shi, H.; Lin, Z.; et al. Driving Factors and Trade-Offs/Synergies Analysis of the Spatiotemporal Changes of Multiple Ecosystem Services in the Han River Basin, China. *Remote Sens.* **2024**, *16*, 2115. [CrossRef]

35. Gong, H.; Li, Y.; Zhang, J.; Zhang, B.; Wang, X. A new filter feature selection algorithm for classification task by ensembling pearson correlation coefficient and mutual information. *Eng. Appl. Artif. Intell.* **2024**, *131*, 107865. [CrossRef]

36. Gocic, M.; Trajkovic, S. Analysis of changes in meteorological variables using Mann-Kendall and Sen's slope estimator statistical tests in Serbia. *Glob. Planet. Chang.* **2013**, *100*, 172–182. [CrossRef]

37. Zhou, R.; Liu, Y.; Wang, X.; Chen, X.; Duan, G.; Han, P.; Lin, Z.; Shi, H.; Wen, Z. Evaluating the effect of Multi-Scale droughts on autumn phenology of global land biomes with satellite observation. *J. Hydrol.* **2024**, *639*, 131547. [CrossRef]

38. Aguilos, M.; Sun, G.; Liu, N.; Zhang, Y.; Starr, G.; Oishi, A.C.; O'Halloran, T.L.; Forsythe, J.; Wang, J.; Zhu, M.; et al. Energy availability and leaf area dominate control of ecosystem evapotranspiration in the southeastern U.S. *Agric. For. Meteorol.* **2024**, *349*, 109960. [CrossRef]

39. Sun, S.; Liu, Y.; Chen, H.; Ju, W.; Xu, C.-Y.; Liu, Y.; Zhou, B.; Zhou, Y.; Zhou, Y.; Yu, M. Causes for the increases in both evapotranspiration and water yield over vegetated mainland China during the last two decades. *Agric. For. Meteorol.* **2022**, *324*, 109118. [CrossRef]

40. Sun, S.; Chen, H.; Sun, G.; Ju, W.; Wang, G.; Li, X.; Yan, G.; Gao, C.; Huang, J.; Zhang, F.; et al. Attributing the Changes in Reference Evapotranspiration in Southwestern China Using a New Separation Method. *J. Hydrometeorol.* **2017**, *18*, 777–798. [CrossRef]

41. Liu, H.; Liu, Y.; Chen, Y.; Fan, M.; Chen, Y.; Gang, C.; You, Y.; Wang, Z. Dynamics of global dryland vegetation were more sensitive to soil moisture: Evidence from multiple vegetation indices. *Agric. For. Meteorol.* **2023**, *331*, 109327. [CrossRef]

42. Bai, M.; Mo, X.; Liu, S.; Hu, S. Contributions of climate change and vegetation greening to evapotranspiration trend in a typical hilly-gully basin on the Loess Plateau, China. *Sci. Total Environ.* **2019**, *657*, 325–339. [CrossRef] [PubMed]

43. Martínez-Lüscher, J.; Kozikova, D.; Goicoechea, N.; Pascual, I. Elevated CO2 alleviates the exacerbation of evapotranspiration rates of grapevine (*Vitis vinifera*) under elevated temperature. *Agric. Water Manag.* **2024**, *302*, 108971. [CrossRef]

44. Ahmadi, A.; Kazemi, M.H.; Daccache, A.; Snyder, R.L. SolarET: A generalizable machine learning approach to estimate reference evapotranspiration from solar radiation. *Agric. Water Manag.* **2024**, *295*, 108779. [CrossRef]

45. Wang, Y.; Li, Z.; Feng, Q.; Si, L.; Gui, J.; Cui, Q.; Zhao, Y.; Xu, C. Global evapotranspiration from high-elevation mountains has decreased significantly at a rate of 3.923 %/a over the last 22 years. *Sci. Total Environ.* **2024**, *931*, 172804. [CrossRef] [PubMed]

46. Zheng, C.; Wang, S.; Chen, J.; Xiang, N.; Sun, L.; Chen, B.; Fu, Z.; Zhu, K.; He, X. Divergent impacts of VPD and SWC on ecosystem carbon-water coupling under different dryness conditions. *Sci. Total Environ.* **2023**, *905*, 167007. [CrossRef]

47. Suliman, M.; Scaini, A.; Manzoni, S.; Vico, G. Soil properties modulate actual evapotranspiration and precipitation impacts on crop yields in the USA. *Sci. Total Environ.* **2024**, *949*, 175172. [CrossRef]

48. Chang, H.; Cai, J.; Xu, D.; Jiang, L.; Zhang, C.; Zhang, B. Precision modelling of leaf area index for enhanced surface temperature partitioning and improved evapotranspiration estimation. *Agric. For. Meteorol.* **2024**, *356*, 110157. [CrossRef]

49. Awada, H.; Sirca, C.; Marras, S.; Castellini, M.; Spano, D.; Pirastru, M. Modelling soil moisture and daily actual evapotranspiration: Integrating remote sensing surface energy balance and 1D Richards equation. *Int. J. Appl. Earth Obs. Geoinf.* **2024**, *128*, 103744. [CrossRef]

50. Yavari Bajehbaj, R.; Cibin, R.; Duncan, J.M.; McPhillips, L.E. Quantifying soil moisture and evapotranspiration heterogeneity within a solar farm: Implications for stormwater management. *J. Hydrol.* **2024**, *638*, 131474. [CrossRef]

51. Shang, S.; Zhu, G.; Zhang, K.; Chen, H.; Wang, Y.; Chen, Y.; Zhang, Z.; Ma, N. Spatial-temporal variations in evapotranspiration across the continental United States: An atmospheric water balance perspective. *J. Hydrol.* **2024**, *640*, 131699. [CrossRef]

52. Gu, C.; Ma, J.; Zhu, G.; Yang, H.; Zhang, K.; Wang, Y.; Gu, C. Partitioning evapotranspiration using an optimized satellite-based ET model across biomes. *Agric. For. Meteorol.* **2018**, *259*, 355–363. [CrossRef]

53. Li, B.; Yang, W.; Wu, X.; Li, Z. Partitioning and controlling factors of evapotranspiration: 2. Dynamics and controls of ratio of transpiration to evapotranspiration at multiple timescales in agroforestry system. *Agric. Ecosyst. Environ.* **2024**, *374*, 109192. [CrossRef]